UNIVERSITÀ DEGLI STUDI DI PADOVA

DIPARTIMENTO DI GEOSCIENZE

UNIVERSITÀ DEGLI STUDI DI PADOVA

SCUOLA DI SCIENZE

DIPARTIMENTO DI GEOSCIENZE

Corso di Laurea Magistrale in Geologia Ambientale e Dinamica della Terra (LM-74)

Curriculum Earth Dynamics

Structural analysis of wrinkle ridges in the region between Aristarchus plateau and Marius Hills in Oceanus Procellarum (Moon)

Relatore: Dr. Riccardo Pozzobon

Correlatore: Prof. Matteo Massironi

Correlatore: Dr. Francesco Mazzarini

Laureando: Giacomo Melchiori

ANNO ACCADEMICO: 2022/2023

Spinning in Daffodils

Abstract

Oceanus Procellarum (Ocean of Storms) represent the largest exposed mare basalts and it is located on the western lunar nearside. The study area of this work is located within this basin, between two big shield volcanoes: the Marius Hills complex and the Aristarchus plateau.

The whole basin is affected by the presence of contractional landforms, known as wrinkle ridges, which are thrust-propagating folds with lengths range from tens to hundreds of kilometres. Since Oceanus Procellarum is a non-mascon (**mass con**centration) basin and, therefore, it is not associated to an excess of subsurface mass, the wrinkle ridges in the study area don't follow a concentric distribution pattern and their strike is mainly in the N-S direction.

596 wrinkle ridges have been mapped with lengths ranging from 1324 m to 150 km, allowing to create a fracture intensity map with tiles size of 100 km * 100 km. A more detailed structural analysis has been carried out: (i) the D_{max}/L has been investigated obtaining a γ value (scaling factor) of about 8.3E-3; (ii) the WRs have been classified by their vergence; (iii) five fault systems of WRs have been identified based on their spatial distribution and for each three parameters have been calculated: the average strike, the spacing, the original spacing; (iv) the décollement depths have been inferred applying the excess area method.

About 75% of the calculated décollement depths ranges between 796 m and 2090 m, these horizons of weakness have been interpreted as paleo-regolith layers formed during hiatus in the volcanic activity of Oceanus Procellarum.

Acknowledgments

I would like to thank my supervisor, Riccardo Pozzobon, without whose competence and patience this thesis project would not have been possible.
I should equally like to thank my co-supervisors, Matteo Massironi and Francesco Mazzarini, for the brilliant conversations we had while writing this thesis.

I would finally like to thank all the people I met during this beautiful path at the University of Padova, some of whom will remain forever.
But I know I'll never lose affection for people and things that went before, and I know I'll often stop and think about them.

Index

1. Introduction

The 20th-century Space Race, during the Cold War, between the United States of America and the Soviet Union, led to pioneering missions and the achievement of ambitious goals for the era such as the first artificial satellite (Sputnik 1), first humans in space (Vostok and Mercury missions) and first humans on the Moon (Apollo missions). After the success of Apollo space program, the competition between U.S.A. and the Soviet Union decreased and the exploration of the Moon was interrupted for fourteen years (1976-1990).

Starting from 1990 different space agencies, such as NASA (National Aeronautics and Space Administration), ESA (European Space Agency), JAXA (Japan Aerospace Exploration Agency) and the CNSA (China Aerospace Science and Technology Corporation) have approached the lunar exploration for scientific purposes.

More recently, **NASA, ESA, JAXA** and **CSA** created the Artemis program which has the purpose to return astronauts to the Moon and, moreover, to establish a sustainable presence on the Moon to prepare for missions to Mars.

Artemis 1 was launched on November 16, 2022, and it was a success, whereas the next missions will include human fly-by and human landing on the Moon.

In this lively context of renewed interest is essential to support the space exploration with scientific studies which can tell us more on the evolution of our satellite. The evolutionary history of the Moon started about 4.5 Ga ago when a Mars-sized object (called Theia) impacted the proto-Earth and the resulting debris re-accreted forming the Moon as a lava planet (Barlow, 1997). From that moment it started to cool forming the high albedo anorthositic highlands and, lately, it suffered a huge phase of bombardment (Late Heavy Bombardment) that was responsible for the creation of the impact basins (lunar maria), which were filled by basalts (Rossi et al., 2018).

Since the Moon lacks plate tectonics (Hauber et al., 2017), its tectonic framework can be ascribed to the two above-mentioned phenomena: (i) the secular cooling at global scale and (ii) at smaller scale the emplacement of thick basal sequences which cause the flexure of the elastic lithosphere (Melosh, 2011). The direct result was the creation of two kinds of contractional landforms: the lobate scarps, which are surface-breaking thrust faults characterized by a global distribution and the

wrinkle ridges, thrust propagating folds, found in lunar maria (Hauber et al., 2017). Thanks to the gravity data obtained from NASA's dual Gravity Recovery and Interior Laboratory (GRAIL) spacecraft it was possible to make high-resolution measurements of the gravity anomalies associated with lunar basins. It is possible to distinguish the positive anomalies due to an excess of subsurface mass (mass concentration or **mascon basins**) as the consequence of impact crater excavation in a still-molten Moon and the subsequent isostatic adjustment during cooling and contraction of melt. On the other hand, the basins characterized by negative gravity anomalies are defined as **non-mascon** basins (Melosh et al., 2013).

The wrinkle ridges in mascon basins follow a concentric distribution pattern related to the presence of thick sequences of mare basalts, which induced subsidence and flexure of the elastic lithosphere (Freed et al., 2001); whereas the wrinkle ridges in non-mascon basins are characterized by non-concentric preferred orientation, the origin of which is still a matter of debate within the scientific community.

Not only the origin, but other aspects need to be further investigated such as: (i) the complex stress field behind their formation which is presumably a result of a combination of different factors; (ii) how the deformation of wrinkle ridges in a certain lunar basin is related to the volcanic and thermal evolution of that basin; (iii) the décollement depths; (iv) the mechanical layering of the crust.

Furthermore, the mapping of these structures has been done only at global scale (Fortezzo et al., 2020) and there is a complete lack of scientific works at basin scale, that would be fundamental to have a solid database on which to do all the needed analysis.

2. Geological Setting

2.1 General Overview

The Moon is the Earth's natural satellite and the largest dwarf planets in the Solar System (Metzger et al., 2022). Our satellite is tidally locked to Earth, and this happens due to the gravitational interaction between the Moon and Earth. This is the reason why the same side of the Moon is always facing Earth (the so-called near side; **Fig.1**).

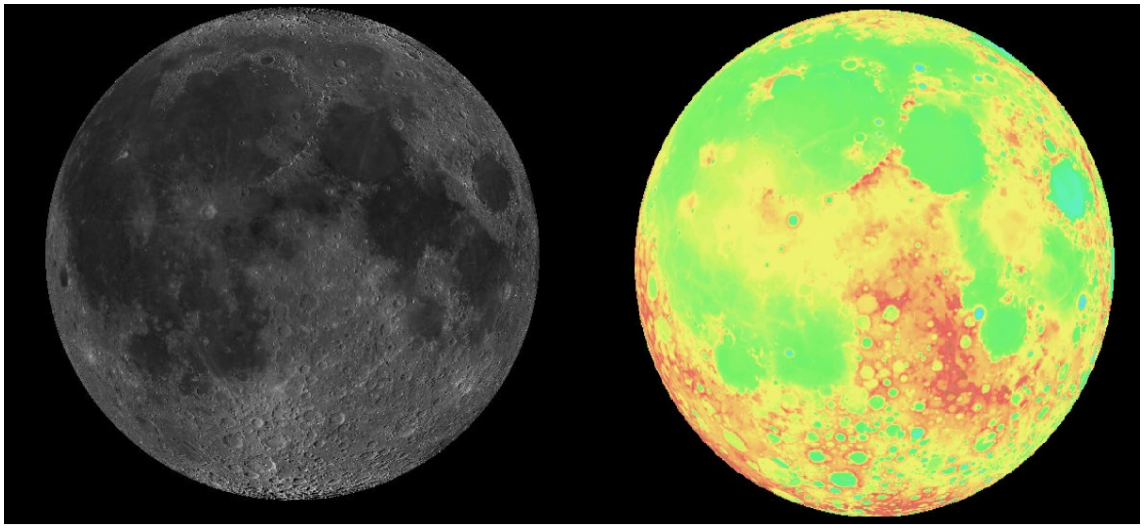

Figure 1. On the left side the near side ("NAC ROI Mosaics" over "NACs large" over "WAC Mosaic", this is a convenience layer that combines LROC NAC high resolution images (0.5 m/pixel) laid over the WAC Global Morphologic basemap (100 meters/pixel); on the right side the Terrain Elevation based on: GLD100 (60S to 60N) + LOLA (60-90), where the GLD100 was produced from Lunar Reconnaissance Orbiter Camera (LROC) Wide Angle Camera (WAC) stereo imagery and LOLA is the Lunar Orbiter Laser Altimeter (LOLA) aboard the Lunar Reconnaissance Orbiter (LRO)

The other feature of the Moon near-side surface, clearly visible from our planet, is the strict dichotomic appearance between the light-toned highlands and the dark so-called maria, that are large, depressed plains (**Fig.1**).

The first attempt to obtain compositional information of the surface of the Moon from the thermal emission spectra was made by Pettit and Nicholson (1930).

In the seventies the thermal emission spectrums of some selected area were measured by Murcray et al. (1970).

More recently, other missions attempted to study the composition of the surface of the Moon, such as the Clementine mission, the SELENE-Kaguya mission, and the Lunar Reconnaissance Orbiter mission.

Clementine was launched in 1994, its purpose was to assess the surface mineralogy of the Moon. The observations included imaging at various wavelengths including ultraviolet and infrared, laser ranging altimetry, and charged particle measurements. Taking advantage of the multispectral imaging it was possible to derive FeO and TiO_2 content of the lunar surface (**Fig.3**) (Lucey et al., 1998).

Afterwards, Kaguya, a Japan's mission (operated by JAXA), was launched in 2007. Among the 14 instruments mounted on board was also present the

Multiband Imager (MI), which is a high-resolution multiband imaging camera with a spatial resolution in visible bands of 20 m and a spatial resolution in near-infrared bands of 62 m from the 100 km orbit altitude. These multispectral images have been used to derive 9 global maps of clinopyroxene, iron, olivine, orthopyroxene, and plagioclase (Lemelin et al., 2015; 2016; 2019).

Lately, with the Diviner Lunar Radiometer Experiment, an instrument flying aboard NASA's Lunar Reconnaissance Orbiter (launched in 2009), it was possible to study the composition of the Moon globally. Greenhagen et al. (2010) analyzed Diviner spectra (**Fig.2**) confirming the mineralogical differences between basaltic maria (pyroxene rich rocks) and the feldspathic highlands (plagioclase feldspar rich rocks).

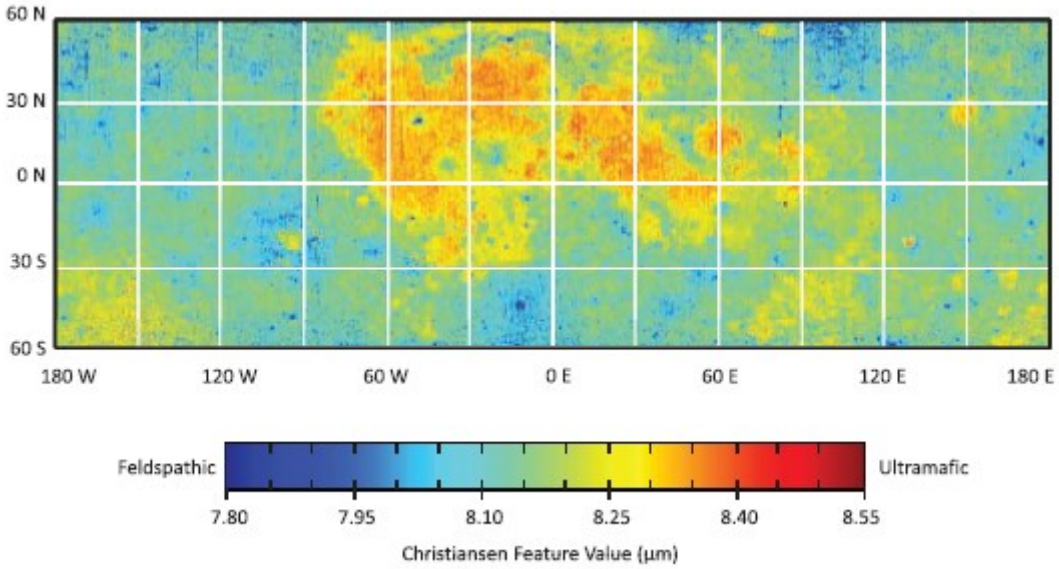

Figure 2. Map showing the composition variability of the lunar terrains (spatial resolution between 8 and 0.5 pixels/degree); the Diviner's8-mm-region channels has been used to characterize a well-studied compositional indicator of silicate mineralogy called the Christiansen feature (CF); modified after Greenhagen et al. (2010).

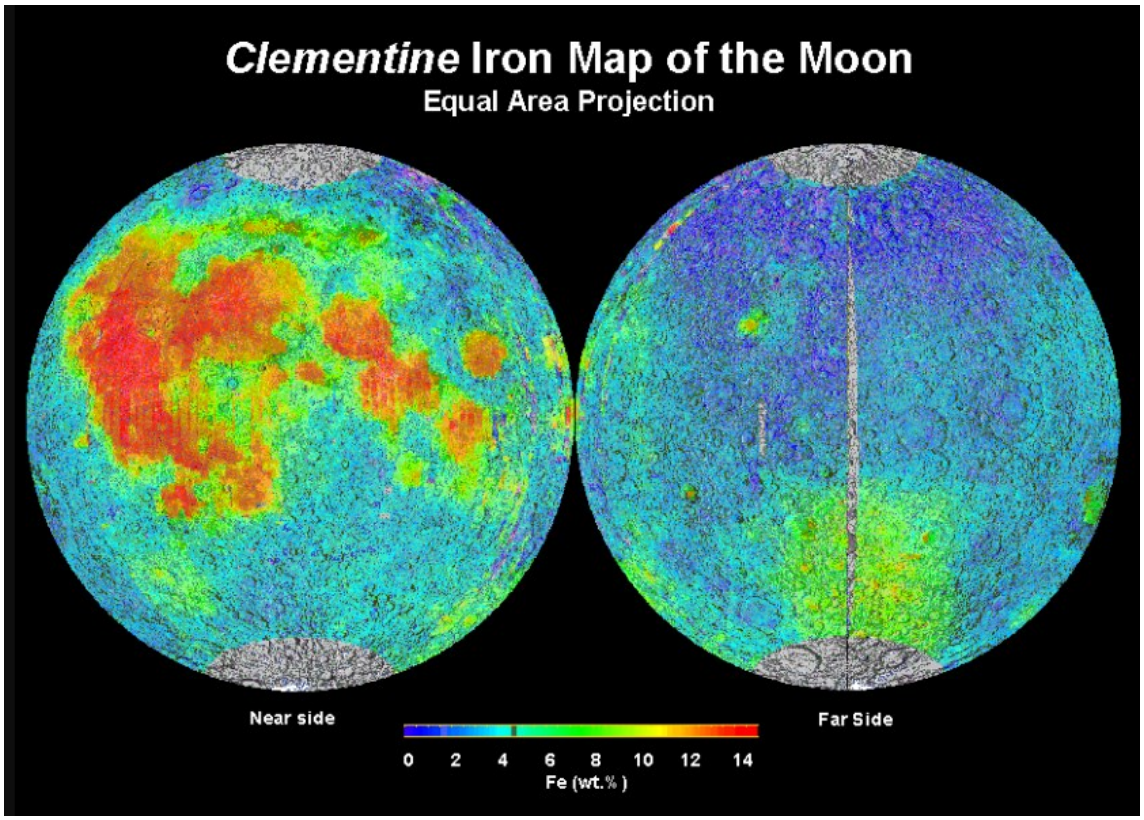

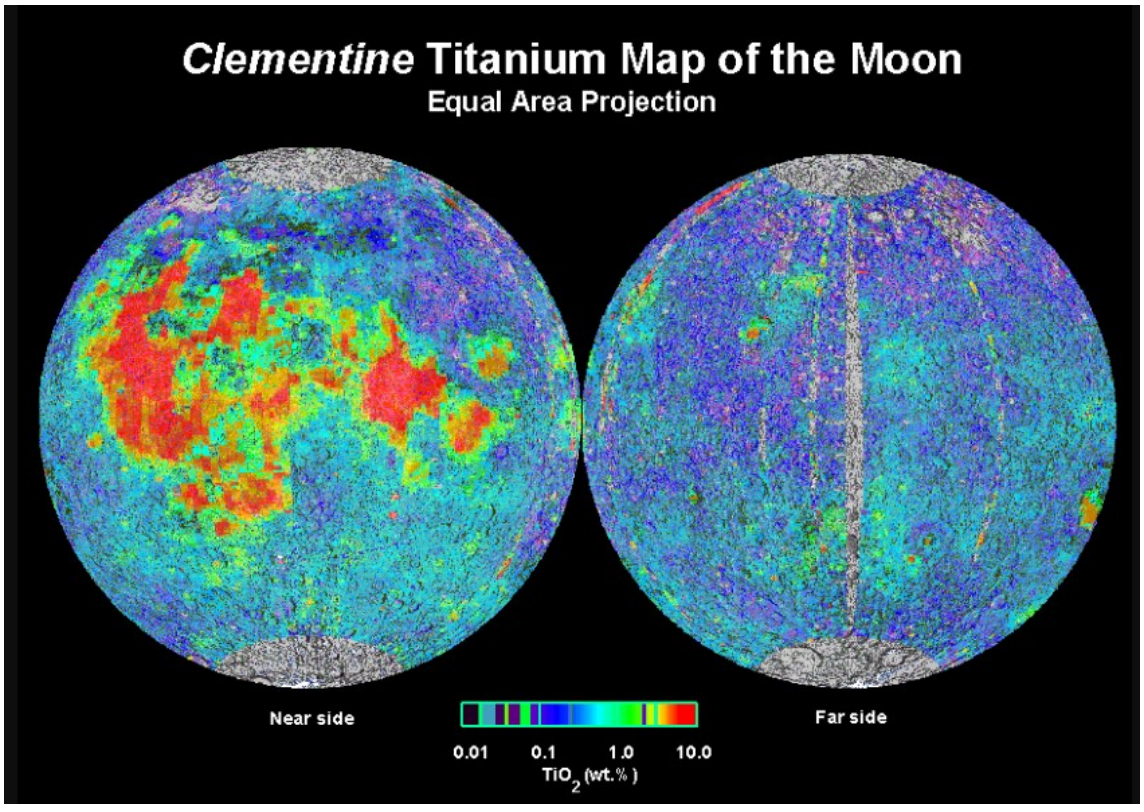

Figure 3. Above image: image derived from the Clementine global colour data (in 750 and 950 nm wavelengths) showing the concentration of iron in the soils of the lunar surface.

Below image: mage derived from the Clementine global colour data (in 415 and 750 nm wavelengths) showing the concentration of titanium in the soils of the lunar surface; images taken from lpi.usra.edu.

More precisely, according to Shearer & Papike (1999) and from the study of the lunar returned samples from Apollo missions and of several lunar meteorites it is well-known that the highlands have a bulk composition equivalent to anorthositic gabbro, whereas the mare basalts consist of volcanic rocks (mainly basalts) enriched in FeO and TiO_2.

2.2 Magmatic Evolution

The Moon and Earth are not only linked by tidal forces, but also from a genetic point of view. The most accredited hypothesis predicts that, during the so-called Early Bombardment (first 0.5 billion years of the solar system history), a Mars-sized object (*Theia*) impacted Earth and the resulting debris re-accreted forming the Moon (**Fig.4**). (Barlow, 1997).

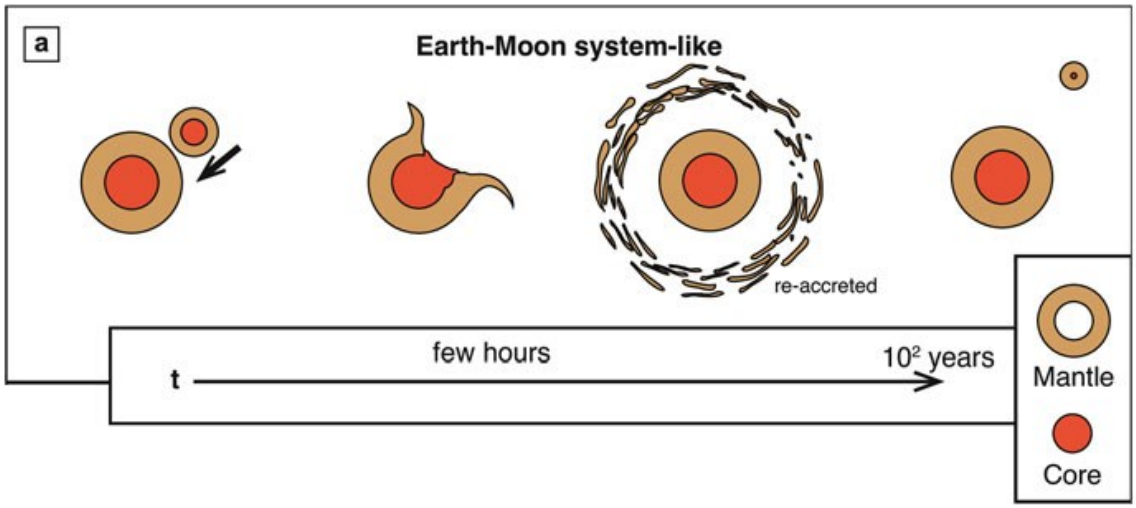

Figure 4. The formation of the Earth-Moon system. Modified after Rossi et al. (2018).

This giant impact led to the formation of a magma ocean, and its subsequent cooling originated the primary crust (Bhutani, 2020).

The magma ocean evolved through fractional crystallization (4.6-3.9 Ga) (Shearer & Papike, 1999). This means that the first minerals to form were the mafic ones (olivine and pyroxene), then the intermediate and the felsic one. Since the mafic minerals were the densest, they sunk at the base of the magma ocean, whereas the lighter feldspars floated at the surface, where they formed the anorthositic primary crust.

In addition, between the crust and the mantle began the accumulation of incompatible elements (**Fig.5**), known as KREEP because of their high levels of

potassium (K), rare earth elements (REE), and phosphorous (P) as revealed by the analysis of the returned lunar samples (Wieczorek & Phillips, 2000).

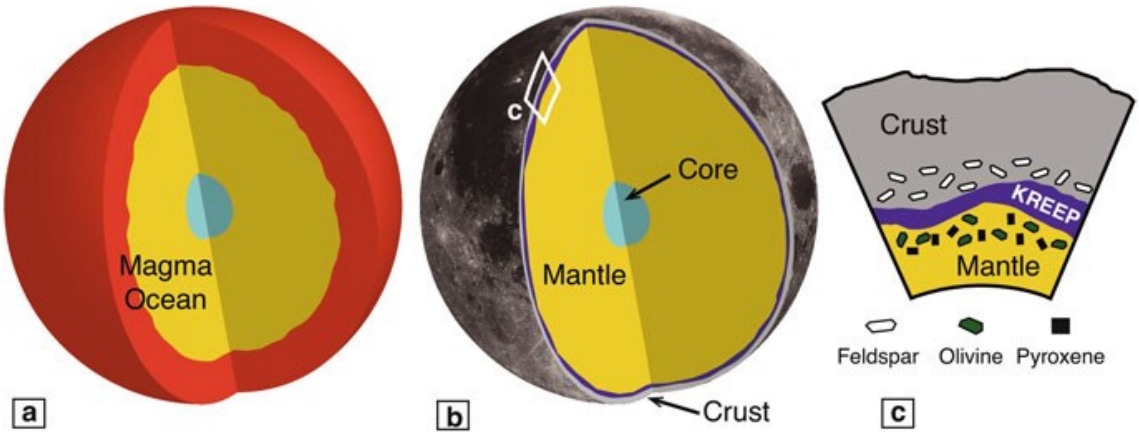

Figure 5. (a) Lunar magma ocean; (b) Final state of the Moon; (c) Incompatible elements are concentrated in the KREEP layer; ,modified after Rossi et al. (2018).

A subsequent phase of bombardment occurred at 3.9-4.0 Gyr (Late Heavy Bombardment), which was related to the gravitational interactions between the planets and the asteroid belt. This phenomenon was responsible for the creation of the impact basins, which are characterized by diameters ranging from hundreds to thousands of kilometres (Rossi et al., 2018).

One of the consequences of the above-mentioned continuous bombardments was the formation of the regolith layer, known also as lunar soil, although it would be more correct to define it as loose material rather than soil (**Fig.6**). The lunar soil is a cohesive, very-fine grained, clastic material derived from the mechanical disintegration of rocks (mainly from impacts); the mean grain size ranges from 40 μm to 800 μm, and the average is between 60 μm and 80 μm (McKay et al., 1991).

Figure 6. Buzz Aldrin's bootprint on lunar soil; by NASA / Buzz Aldrin.

After the formation of an early anorthositic crust (the present-day highlands) the partial melting of the mantle produced a secondary crust (basalts), which can be found in the large impact basins (**Figs, 7, 8**) (Rossi et al., 2018).

The formation of basalts in the Moon took place in an environment characterized by different physical and chemical properties, furthermore they are depleted in volatile elements, with no or only a little percentage of water (Spudis, 2015). Probably, these huge plains of basaltic lava were emplaced through fissure-fed, flood-style eruptions (Spudis et al., 2013).

On Earth and on other planets this kind of eruptions are related to the presence of big shield volcanoes, where the term “shield volcanoes” indicates positive-relief volcanic constructs that have very low positive slopes. These kinds of volcanic

edifices (e.g., the Marius Hills Complex and the Aristarchus Plateau) have recently been confirmed by Spudis et al. (2013) using topographic data from the LOLA (Lunar Orbiter Laser Altimeter) and LROC (Lunar Reconnaissance Orbiter Camera instruments).

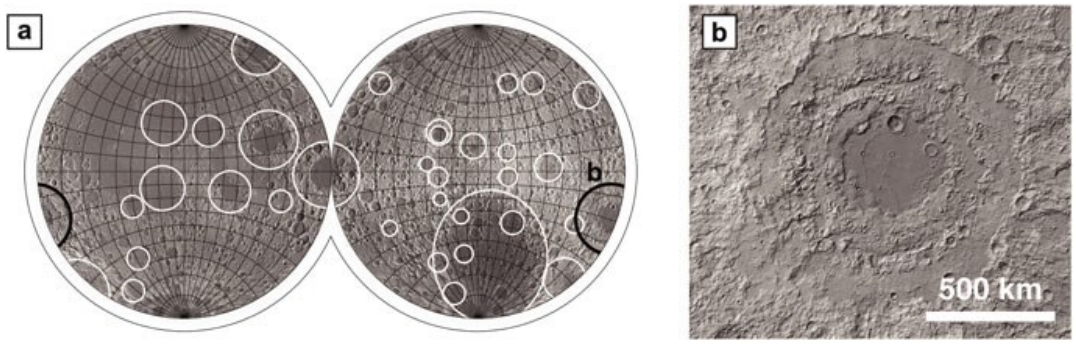

Figure 7. (a) Basins formed around 3.9Gyr ago; (b) The lunar Orientale basin. Modified after Rossi et al. (2018).

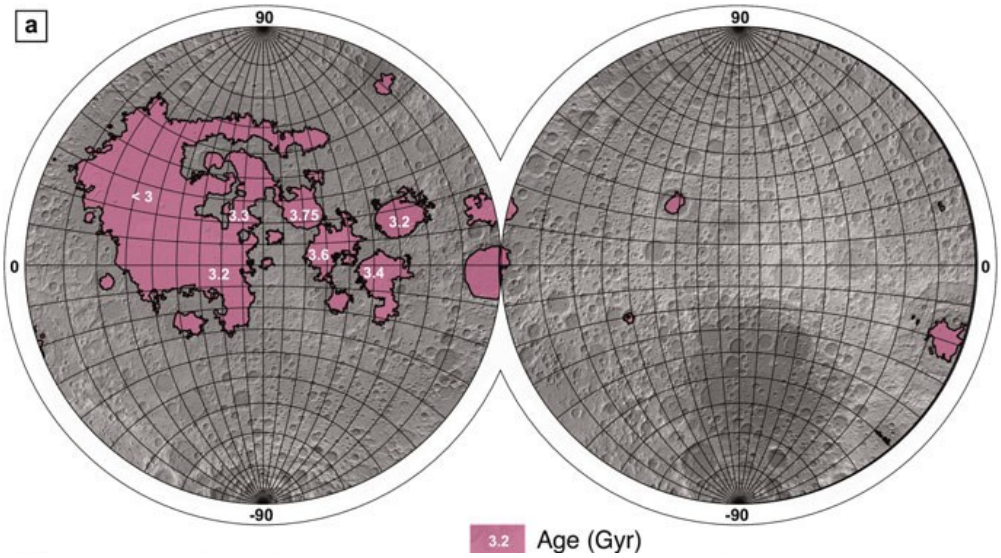

Figure 8. Secondary crusts on the lunar surface. Modified after Rossi et al. (2018).

Lunar basalts exhibit a wide range of compositions that resulted from near-surface fractionation of primary basaltic magmas. They are enriched in FeO and TiO_2 and three major groups have been identified: high-Ti basalts (>9% wt TiO_2), low-Ti basalts (1.5-9% wt TiO_2), and very low Ti-basalts (<1.5% wt TiO_2) (Taylor et al., 1991).

Even if in the past it was thought that the magma emplacement in lunar basins occurred during massive events or as a fractionated lava lake deposit, lately, the idea of multiple, low-rate effusion events, forming compound units (**Fig.9**) has

been proposed for Oceanus Procellarum and others maria (Robinson et al., 2014) (Weider et al., 2010).

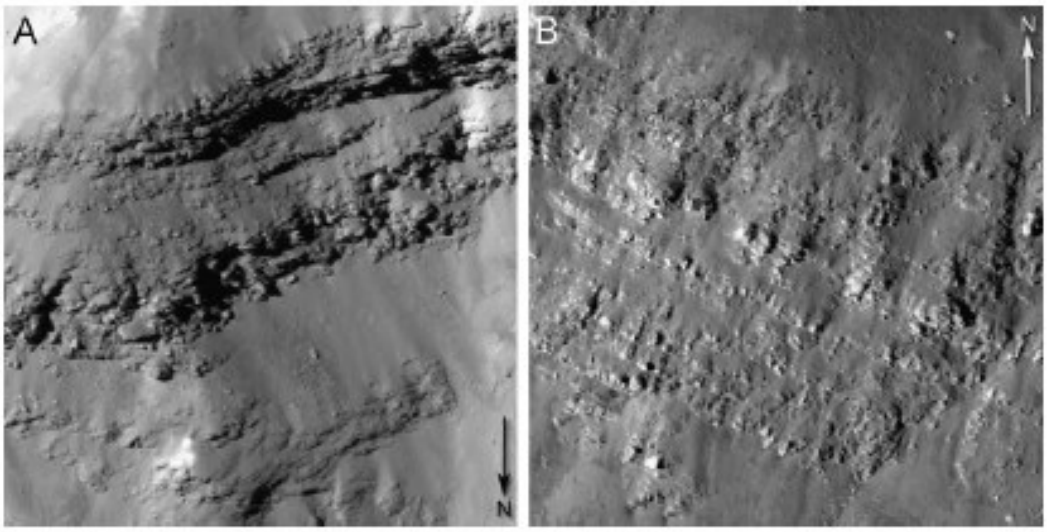

Figure 9. Horizontal striations in crater walls indicate mare flow thickness of 2 to 5 m (Kepler crater); modified from Robinson et al. (2012).

In addition, the magmatic activity was not continuous through time, but it was characterized by several hiatus resulting in the formation of layers of regolith due to the continuous bombardment that the Moon underwent through time (the so-called paleo-regolith). The presence of these layers has been confirmed by the Chinese robotic spacecraft mission Chang'e 4, which landed on the floor of the Von Karman crater on the dark side of the Moon in the South-Pole Aitken basin, where it started to analyse the subsurface thanks to its dual-channel lunar penetrating radar (LPR) (Zhang et al., 2020).
The LPR includes two channels:

- low frequency channel (CH-1, 60 MHz);
- high frequency channel (CH-2; 500 MHz).

The CH-1 investigated the subsurface structure to a depth of hundreds of meters, whereas the CH-2 detected the shallow lunar regolith structure (Zhang et al., 2020). It has been possible to reconstruct the stratigraphy underneath the Von Karman crater from the surface to a depth of 350 meters (Zhang et al., 2020).
As **figure 10** shown, the most interesting aspect is the presence of:

- alternating layers of ejecta between 12-50 m;

- a layer of paleo-regolith between 110-130 m;
- another layer of paleo-regolith between 158-163 m;
- a layer of ejecta between 263-280 m.

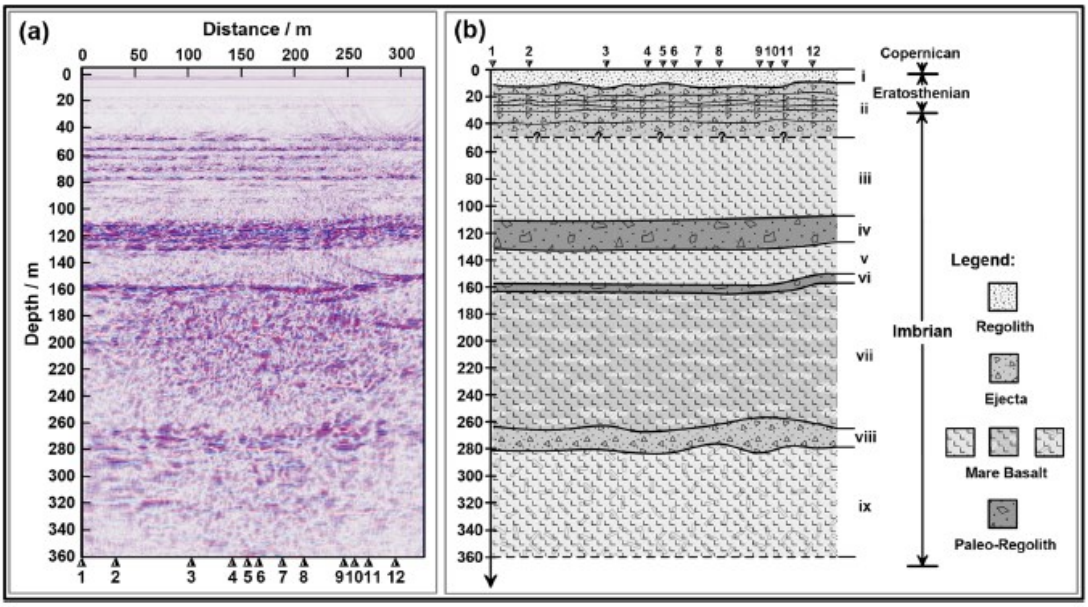

Figure 10. Result and interpretation of the CH-1 data. (a) The initial results of CH-1 data. (b) Proposed stratigraphy of the CE-4 landing site; modified from Zhang et al. (2020).

Another proof of the presence of paleo-regolith layers is provided by the work of Bando et al. (2015) which studies subsurface stratification beneath Reiner Gamma and Mare Imbrium (**Fig.13**) using the Lunar Radar Sounder (LRS) onboard the Kaguya spacecraft, which takes advantage of the penetration ability of electromagnetic radar waves.

They modelled the two-way propagation (space-mare basalts), and they obtained two-end members (**Fig.12**):

- (a) the presence of subsurface paleo-regolith;
- (b) the presence of ejecta blanket.

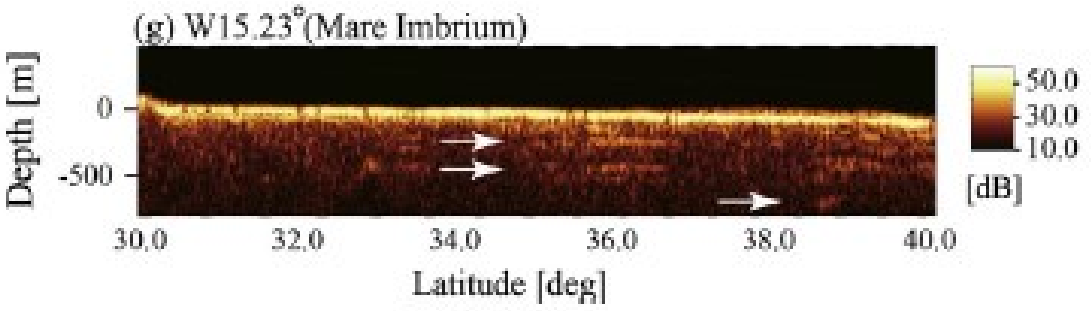

Figure 11. Subsurface feature (depth versus latitude) beneath Mare Imbrium, which are SAR-processed radargrams, the white arrows are indicating two reflectors that have the dielectric constant of lunar regolith (ε=3.3); modified from Bando et al. (2015).

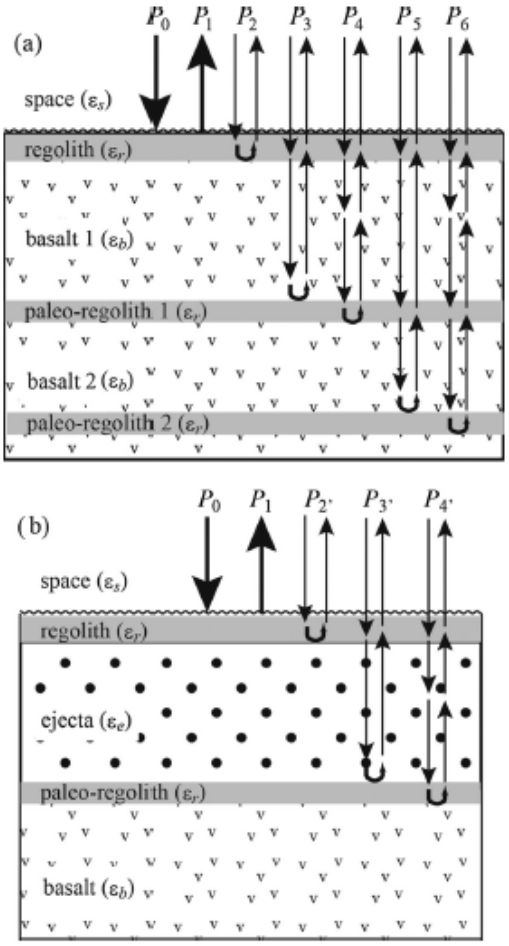

Figure 12. Two attenuation models for the transmission and reflection of electromagnetic waves of LRS in the lunar subsurface and surface boundary contacts where P_0 is the incident power of LRS; and P_1, P_2, P_3, P_4, P_5 and P_6 represent the reflected power; and ε is the dielectric constant; modified from Bando et al. (2015).

It has not been possible to observe any precise layering beneath Rainer Gamma, but some reflectors have been identified beneath Mare Imbrium (**Fig.11**) with the dielectric constant (ε) of regolith (ε=3.3).

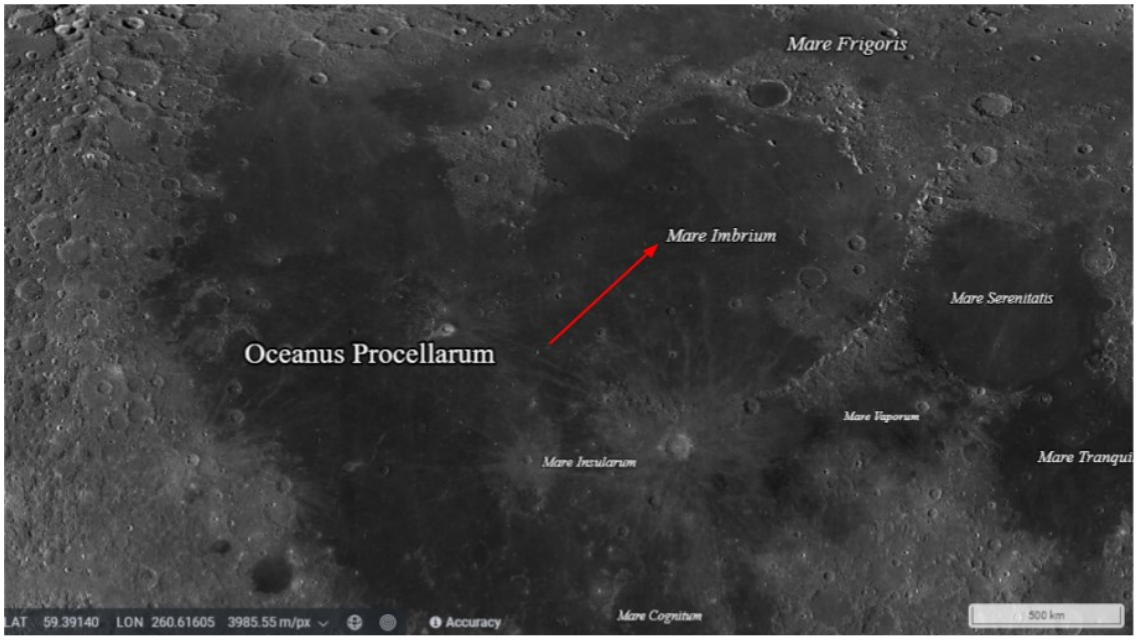

Figure 13. The red arrow is showing where the radar acquisition was made in Mare Imbrium; image taken from quickmap.lroc.asu.edu.

From a temporal point of view, volcanic activities lasted up to about 3 billion years and the last 1 Ga was characterized by impact bombardment and small-scale volcanic activity (Rossi et al., 2018). The decrease in volcanic activity of a planet over time is related to the fact that the duration of volcanic activity is related to their relative size, mass, and heat capacity (Rossi et al., 2018).

A more detailed description and characterization of lunar basins has been done thanks to the gravity data obtained from NASA's dual Gravity Recovery and Interior Laboratory (GRAIL) spacecraft. Using GRAIL data, it was possible to make high-resolution measurements of the gravity anomalies associated with lunar basins. It is possible to distinguish the positive anomalies due to an excess of subsurface mass (hereinafter referred to **mascon basins**) as the consequence of impact crater excavation in a still-molten Moon and the subsequent isostatic adjustment during cooling and contraction of melt (Melosh et al., 2013). On the other hand, the basins characterized by negative gravity anomalies are defined as **non-mascon** basins (**Fig.14**).

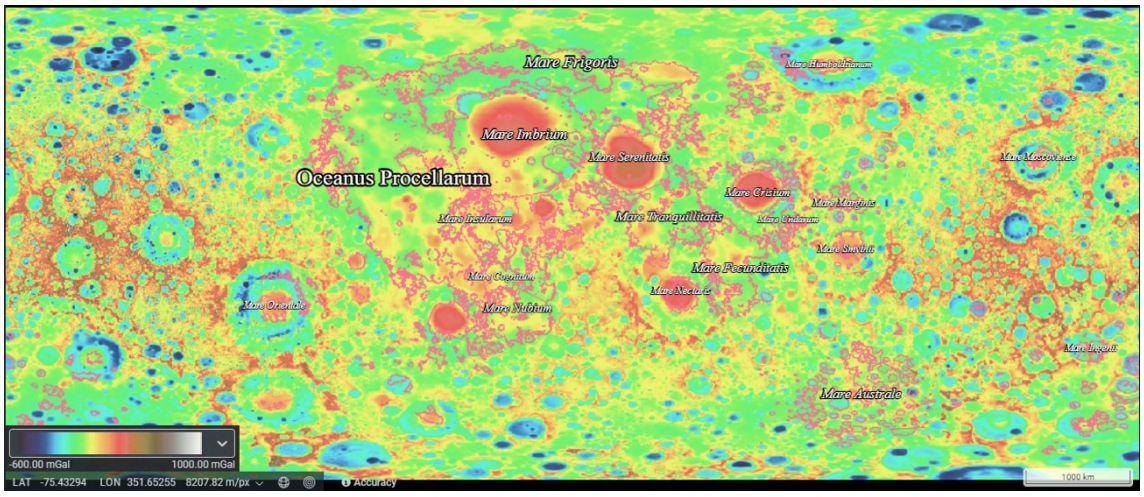

Figure 14. GRAIL free air gravity (mGal) or gravity disturbances at 16 pixels/degree computed at the reference radius of 1738 km using the GRGM1200A gravity model at expansion degree L=660. In magenta the lunar maria boundaries. Image taken from quickmap.lroc.asu.edu.

2.3 Tectonism on the Moon

The Moon can be seen as a one-plate planet (Hauber et al., 2017), whose global tectonic evolution is to be attributed to the following factors (**Fig.15**):

- The secular heating (global expansion) and cooling (global contraction);
- The orbital despinning: as the rotation rate decreases the polar radius will increase (extensional structures), whereas the equatorial radius will decrease (contractional structures).

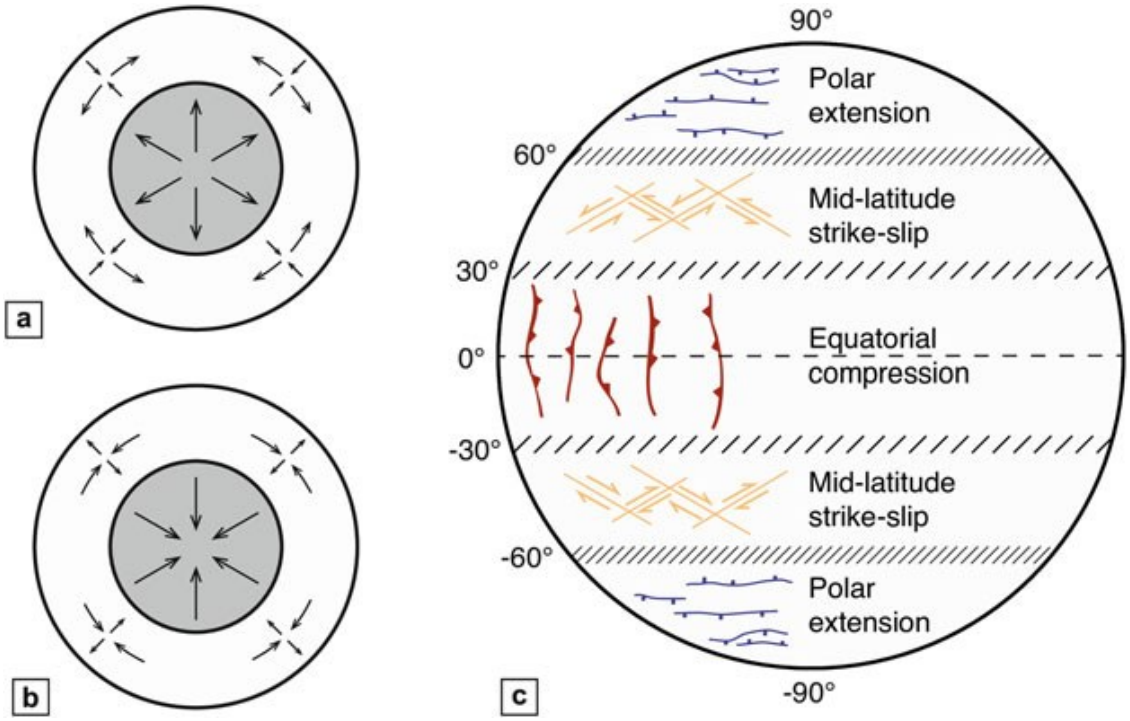

Figure 15. (a) Initial global heating and expansion, with dominant lateral tensional stresses in the crust. (b) Late-stage global cooling and contraction. (c) Predicted global tectonic pattern of a despinning planet; modified from Hauber et al. (2017).

At smaller scale the lunar surface is shaped by the impacts of objects moving at many kilometres per second which can excavate basins (impact cratering) (Melosh, 2011).

The side effects related to this phenomenon are:

- The emplacement of magma within the excavated basin (thanks to dikes and sills);
- The creation of stresses once the magma has cooled and loaded the crust;
- The flow of underlying viscous mantle material beneath the basin's center (Melosh, 2011).

The above-mentioned factors represent the most common sources of stresses which determined the formation of two kinds of contractional structures: **wrinkle ridges** and **lobate scarps**.

Lobate scarps are simple landforms with steeply sloping faces and more gently sloping back limbs (**Fig.16**) which have a global distribution (Banks et al., 2012). They are shallow thrust faults with dip angles of <36°; in plain view, as their name suggest, are lobate, often slightly curvilinear with en-echelon scarp segments

geometry. Multiple studies inferred that these structures could form due to a small radial contraction, plus, they are consistent with the Lunar Magma Ocean (LMO) thermal model (Clark et al., 2017).

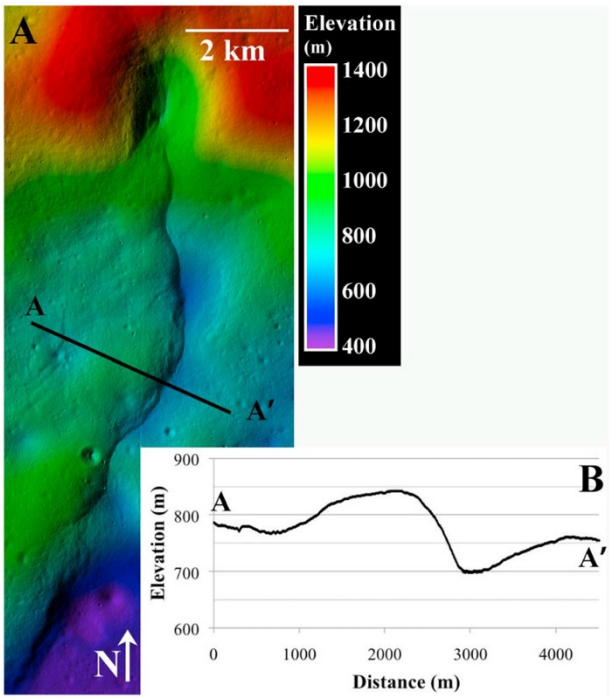

Figure 16. (a) DTM from NAC stereo images) of a lobate scarp; (b) Profile across the lobate scarp; modified from Banks et al. (2012).

On the other hand, **wrinkle ridges** (thrust-propagation folds) (Hauber et al., 2017) are concentrated in maria (lunar basins) (**Fig.17**).

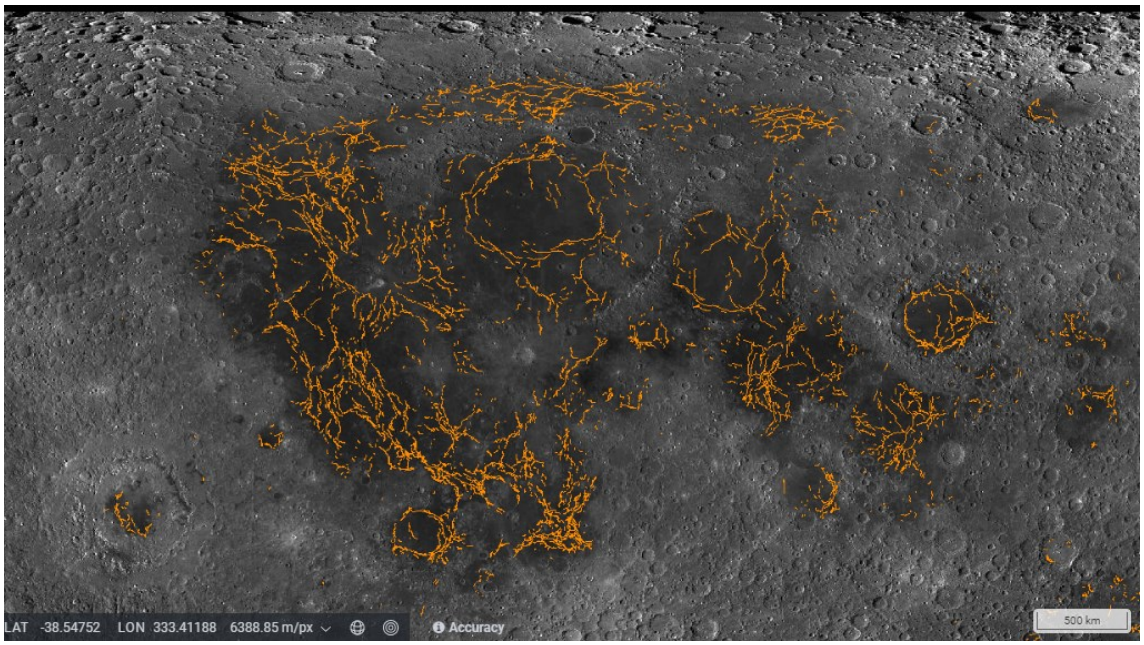

Figure 17. The orange lines represent the wrinkle ridges on the lunar surface which are concentrated in maria; image taken from quickmap.lroc.asu.edu.

The possible mechanism of formation of wrinkle ridges localized within **mascon** basins involved the isostatic loading of the lunar lithosphere; on the other hand, in **non-mascon** basins, they showed preferred orientation which appear to be the result of the combination of several factors, such as: global contraction, lunar orbital recession and solid body tides (Watters et al., 2015).

Because the contractional features show a non-random distribution of orientations, instead of a random distribution as required for the global contraction model, the model that considers several factors contributing to the formation of wrinkle ridges is more considered.

For these reasons it is inferred that 3 different stress components are acting on the lunar crust (Watters et al., 2015):

- σ_c related to global contraction.
- σ_r related to orbital recession stress
- σ_t related to diurnal tidal stress.

Where $\sigma_c \gg \sigma_r > \sigma_t$.

According to numerical models (Watters et al., 2015), even if the diurnal tidal and the orbital recession stresses are small compared to the global contraction stress, they are high enough to generate contractional features with non-random orientations (**Fig.18**).

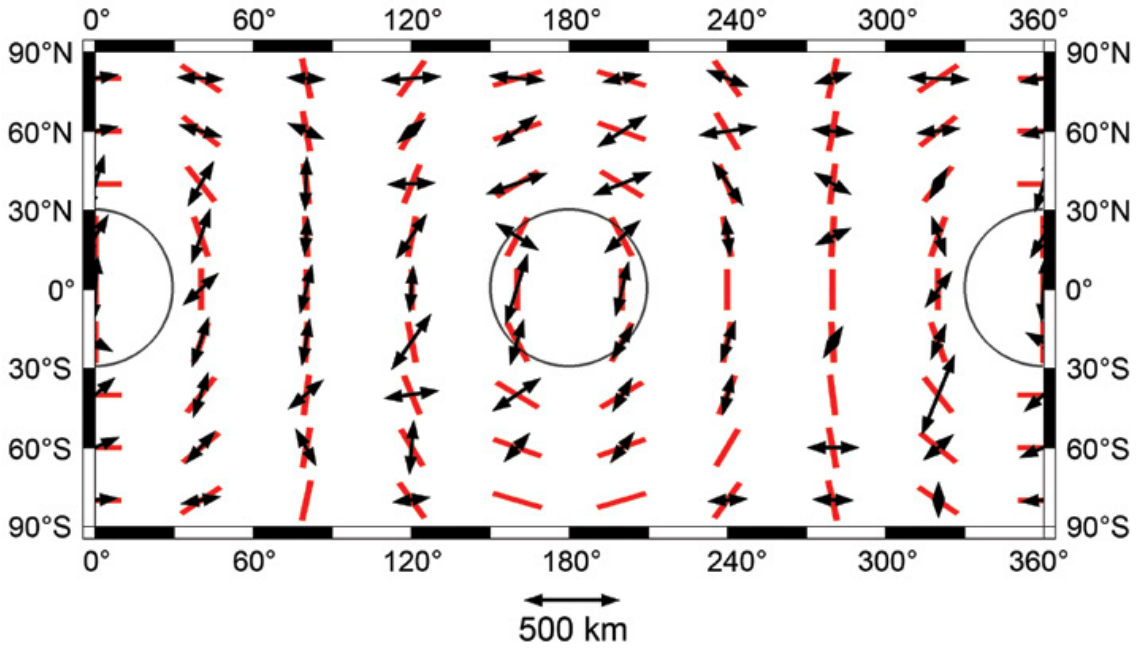

Figure 18. Orientations of predicted faults (red lines) due to combination of recession stresses, diurnal tidal stresses at apogee, and global contraction plotted with median orientations of lobate scarps (black double arrows); from Watters et al. (2015).

The relationship between the maximum displacement (D_{max}) and the length (L) of **wrinkle ridges** has been investigated for mascon and non-mascon basins (Watters, 2022).

$$D_{max} = \gamma L^n$$

Where **γ** is called **scaling factor** and **n** refers to the rate of displacement accumulation related to **L.**

Different fault population will have different value of γ and n, which, in turn, are related to different factors, such as lithology, fault geometry, friction and stress state. Contrasting γ values are expected for mascon and non-mascon basins, but they are undistinguishable (**Fig.19**) (Watters, 2022).

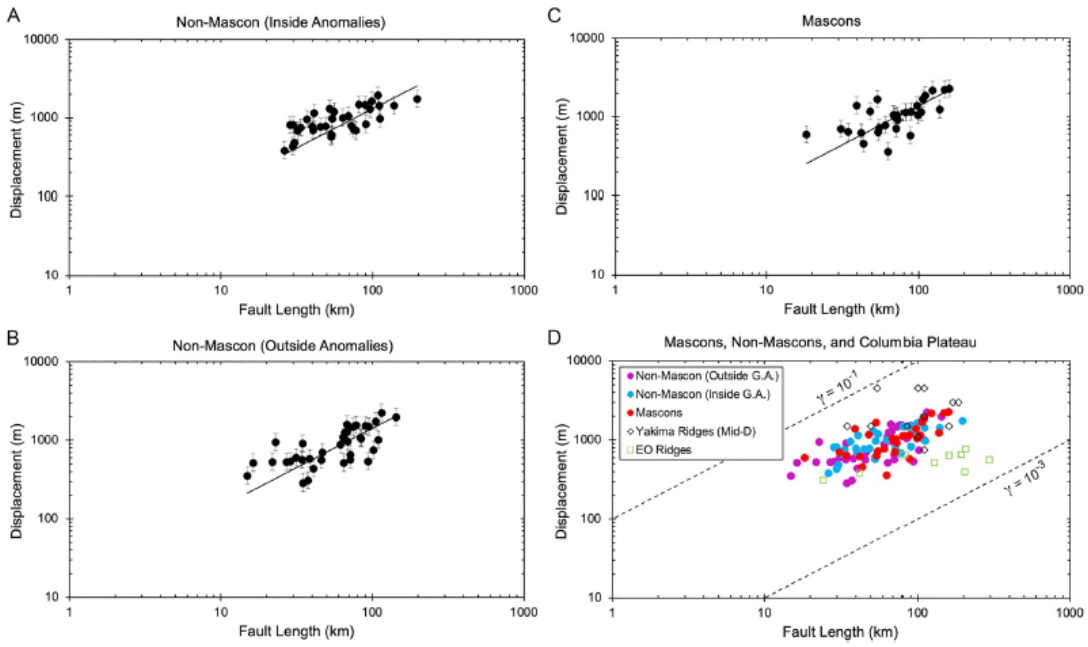

Figure 19. Displacement-length plots of lunar wrinkle ridges in various settings. (a) *Dmax/L* plot of wrinkle ridges where Gravity Recovery and Interior Laboratory gravity gradient anomalies are in non-mascons (γ = 1.31 × 10 −2). (b) *Dmax/L* plot of wrinkle ridges outside areas where gradient anomalies are located (γ = 1.42 × 10 −2). (c) *Dmax/L* plot of wrinkle ridges in mascon settings (γ = 1.38 × 10 −2). (d) *Dmax/L* plot of all lunar wrinkle ridges examined in this study (γ = 1.37 × 10 −2) along with *Dmax/L* estimates for elevation offset ridges. The Yakima ridges of the Columbia Plateau are also plotted using midrange estimates of the displacement; modified from Watters (2022).

Watters (2022) proposed that a thinner elastic lithosphere in non-mascon allowed thinner sequences of mare basalt to form wrinkle ridges with γ values comparable to those of mascon basins.

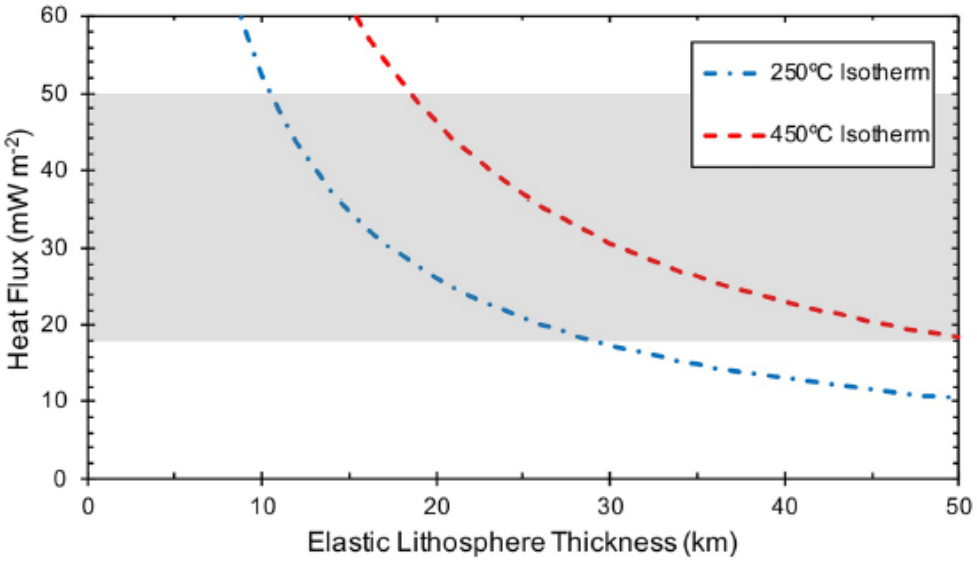

Figure 20. Elastic litosphere thickness as function of the heat flux; modified from Watters (2022).

The elastic lithosphere thickness is function of the heat flux (**Fig.20**) and, thanks to the measured heat flow at Apollo 15 and Apollo 17 landing sites (**Fig.21**), it has been inferred that the highest heat flux on the Moon occurs in the Oceanus Procellarum (the biggest non-mascon basin). Thus, such a high heat flux results in a very thin elastic lithosphere in agreement with the model of Watters (2022).

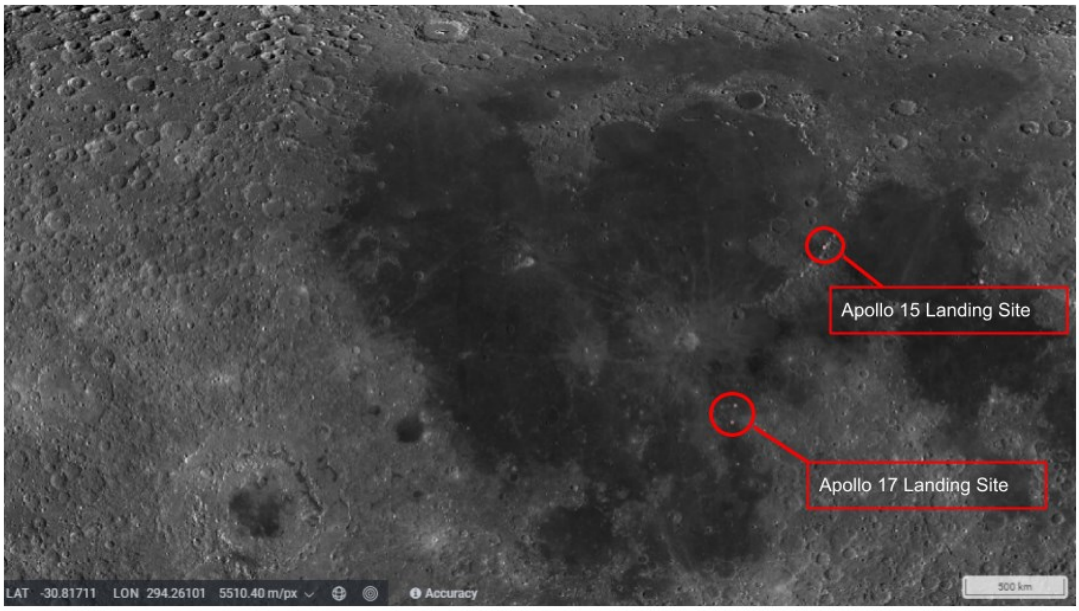

Figure 21. The landing site of Apollo 15 and 17 on the border of Oceanus Procellarum; taken from quickmap.lroc.asu.edu.

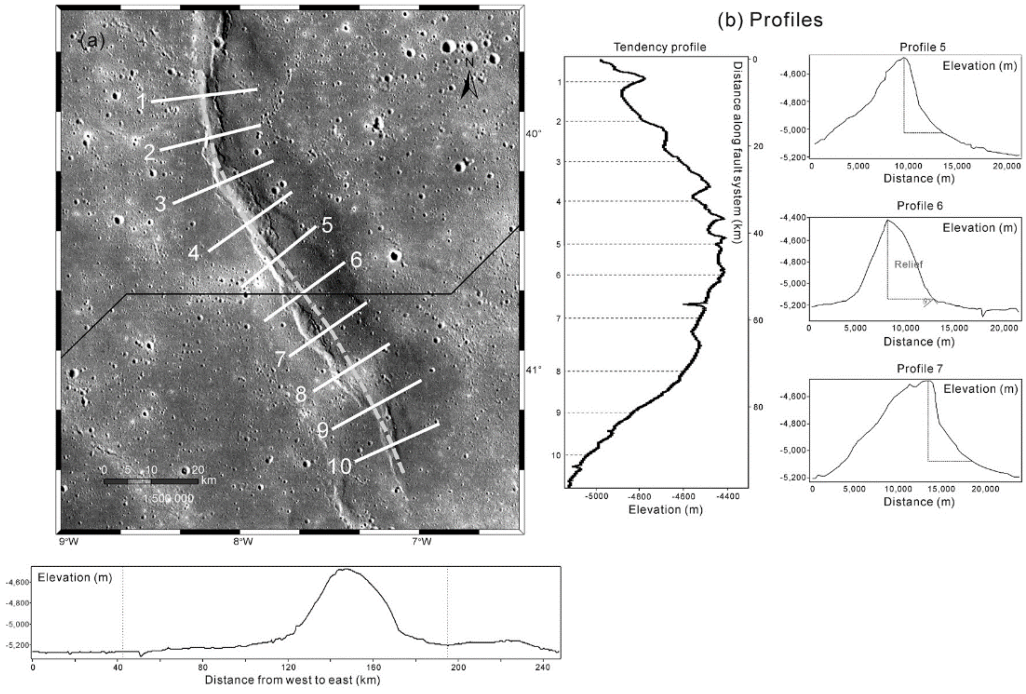

Figure 22. (a) Topographic map of the selected wrinkle ridge in Mare Imbrium and its east-west profile below. (b) The profiles, including the along-strike profile and topographic profiles 5, 6 and 7. Modified after Li et al. (2023).

The morphology of the wrinkle ridges shows that they are low-relief structures, from straight to curved in plan-view with length vary from tens to hundreds of kilometres. In cross-section they are usually asymmetric, with the forelimb (vergent side, i.e., the side toward the transport direction) steeper with respect to the back-limb which shows gentler slopes. This morphological difference gives us information on their vergence (**Figs 22** and **23**).

On the Earth the dip angle for thrust faults ranges from 15° to 45° (Olson, 2003; Grasemann et al., 2011; Stanton-Yonge et al., 2020; Wei et al., 2020). Byrne et al. 2015 estimated with a finite-element model analysis that dip angles for wrinkle ridges on the Moon are ranging from 5° to 25°.

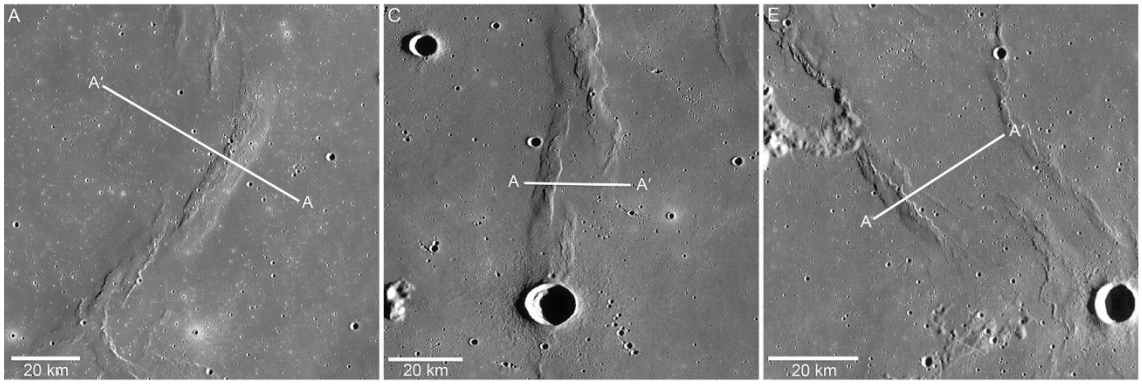

Figure 23. (a) Lunar Reconnaissance Orbiter Camera (LROC) Wide Angle Camera (WAC) mosaic of Dorsa Lister in Mare Serenitatis (21.0°N, 24.54°E); (c) LROC WAC mosaic of a wrinkle ridge in Mare Imbrium (35.76°N, 31.36°W); (e) LROC WAC mosaic of a wrinklel ridge in Procellarum (4.85°S, 48.0°W). Modified after Watters. (2022).

Their formation occurred over a long period of time, Yue et al. (2017) inferred that they started forming about 4 Ga ago, with a peak between 3.5 Ga and 3.1 Ga continuing until 1.2 Ga.

2.4 Lunar Geologic Timescale

The selenological timescale (**Fig.24**) divides the Moon's geological history into 5 periods: **Copernican**, **Eratosthenian**, **Imbrian**, **Nectarian**, and **Pre-Nectarian**, respectively [Ding & Xu, 2019].

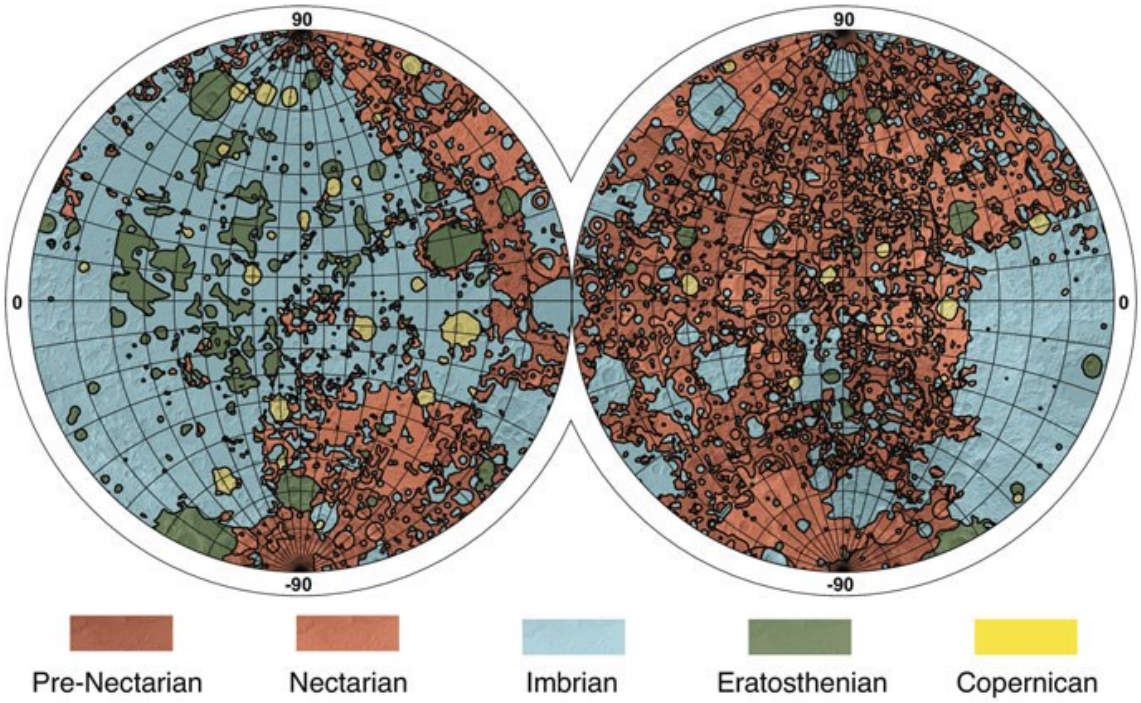

Figure 24. Global surface ages. Modified after Rossi et al. (2018).

Pre-Nectarian (4.56-4.0 Ga)

It defines the period between the formation of the lunar crust and the time of the Nectaris impact event, its ejecta blanket serves as a stratigraphic marker. Primitive magma ocean formed.

Nectarian (4.0-3.92 Ga)

It defines the period between the formation of the Nectaris and Imbrium impact basins.

Imbrian (3.92-3.16 Ga)

It has been subdivided into *Early* (3.92-3.80 Ga) and *Late* (3.80-3.16 Ga) epochs. The Early Imbrian defines the time between the Imbrium and Orientale impact basins; the Late Imbrian defines the time between the formation of the Orientale basin, and large-scale effusion of basalt filling basins and craters [Liu & Guo., 2018]

Eratosthenian (3.16-1.1 Ga)

The main geological feature that characterizes this period regard a reduction in the frequency of impacts with craters becoming smaller.

Young craters with *ray system* subdued were formed and small-scale basalts (very low volumes of magmas) filled in basins and craters [Liu & Guo., 2018].
A *ray system* comprises radial streaks of fine ejecta thrown out during the formation of an impact crater.

Copernican (1.1-present Ga)

It is defined by the formation of the Harplus crater and in addition, craters with preserved ray system were formed.

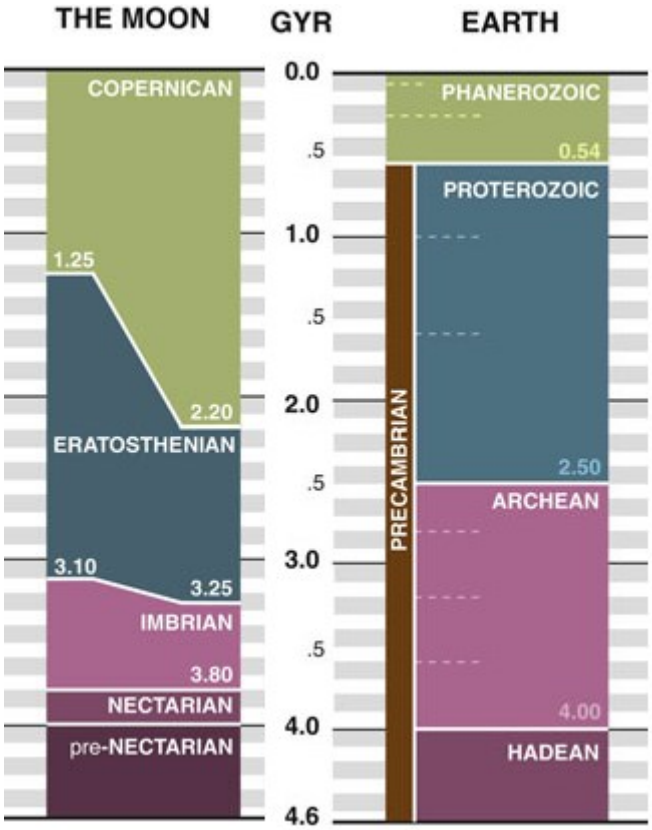

Figure 25. Chronostratigraphic comparison between the Moon and Earth. Modified after Rossi et al. (2018).

2.5 Maria Nomenclature

As mentioned in the introduction the lunar maria are dark, basaltic plains formed by impacts (**Fig.26**).
They are called *maria* (Latin for 'seas') because the early observers thought they were seas. The whole nomenclature for the Moon follows this idea including terms like oceanus, lacus, palus and sinus.

The names of maria can refer to sea features (Mare Imbrium, Mare Frigoris, etc.), sea attributes (Mare Australe, Mare Orientale, etc.) or states of mind (Mare Serenitatis, Mare Tranquillitatis, etc.)

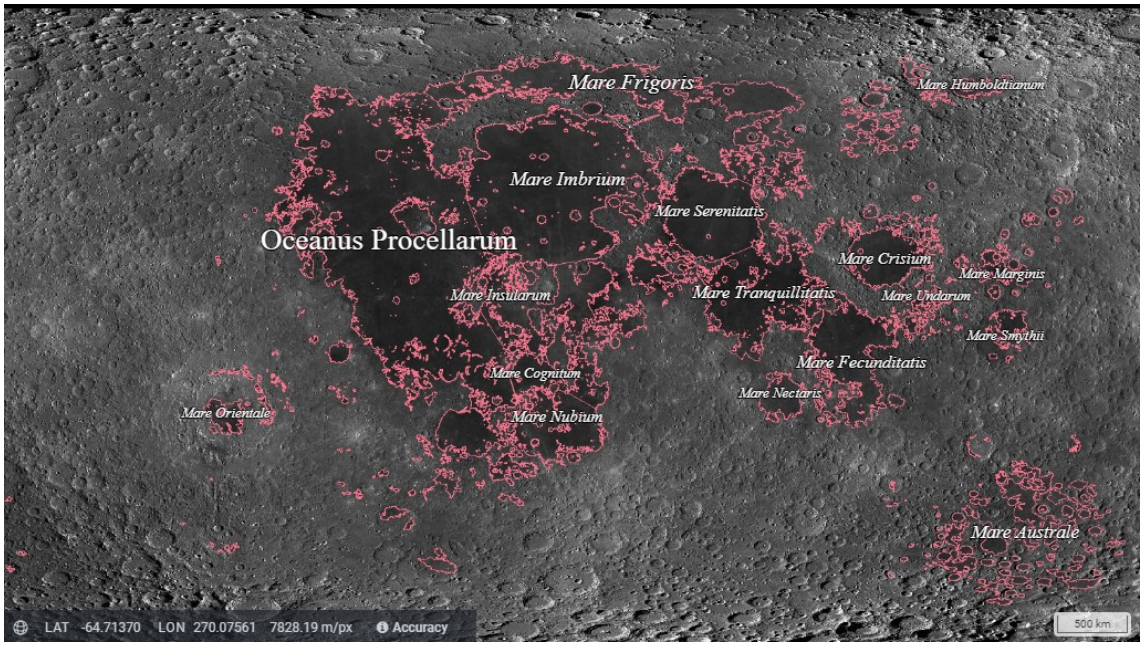

Figure 26. The lunar maria bounded by pink lines. Image taken from quickmap.lroc.asu.edu.

2.6 Oceanus Procellarum

The only lunar maria to be called Oceanus due to its size is **Oceanus Procellarum** (Ocean of Storms).

It is located on the western lunar nearside (**Northernmost Lat:** 57.43°; **Southernmost Lat:** -16.27°; **Easternmost Long:** -26.85°; **Westernmost Long:** -81.08°; CRS: Planetographic, +East, -180 - 180) and it has a non-circular shape (**Fig.27**); some authors (Hiesinger, 2003; Wilhelms and McCauley, 1971; Whitaker, 1981; Wilhelms, 1987) interpreted it as a large impact structure, whereas other authors are not yet convinced about this hypothesis due to the difficulty in identifying the ring structures of this basin (Hiesinger, 2003; Spudis, 1993; Spudis and Schultz, 1985; Wilhelms, 1987).

Fig 27. Oceanus Procellarum ("NAC ROI Mosaics" over "NACs large" over "WAC Mosaic"); image taken from quickmap.lroc.asu.edu.

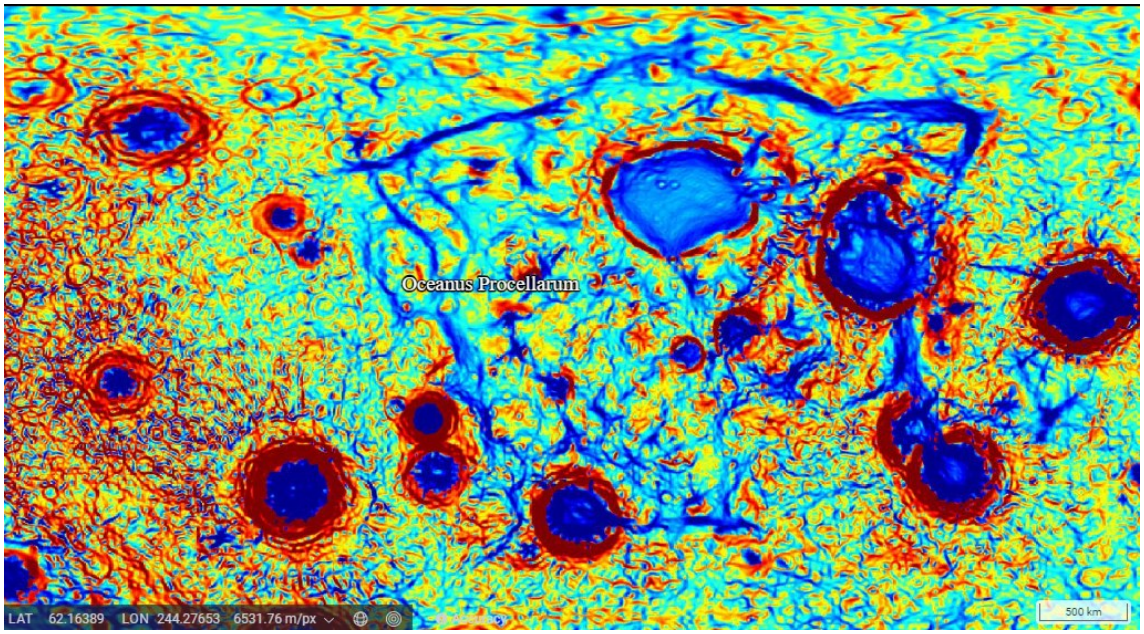

Figure 28. Oceanus Procellarum ("Bouguer gravity gradients derived from GRAIL Bouguer gravity model"); the gravity gradients contain the maximum amplitude eigenvalue of the second horizontal derivative of the Bouguer potential at each point on the surface, as described in the Supplementary Materials of Andrews-Hanna et al. [2014]; image taken from quickmap.lroc.asu.edu.

The Oceanus Procellarum has always aroused great scientific interest, because, because it is a **non-mascon basin** and **the largest exposed mare basalts** (**Fig.28**).

The study area of this work is in Oceanus Procellarum, and it includes two big and well-known shield volcanoes: the Marius Hills complex and the Aristarchus plateau (**Fig.29**) (Spudis et al., 2013).

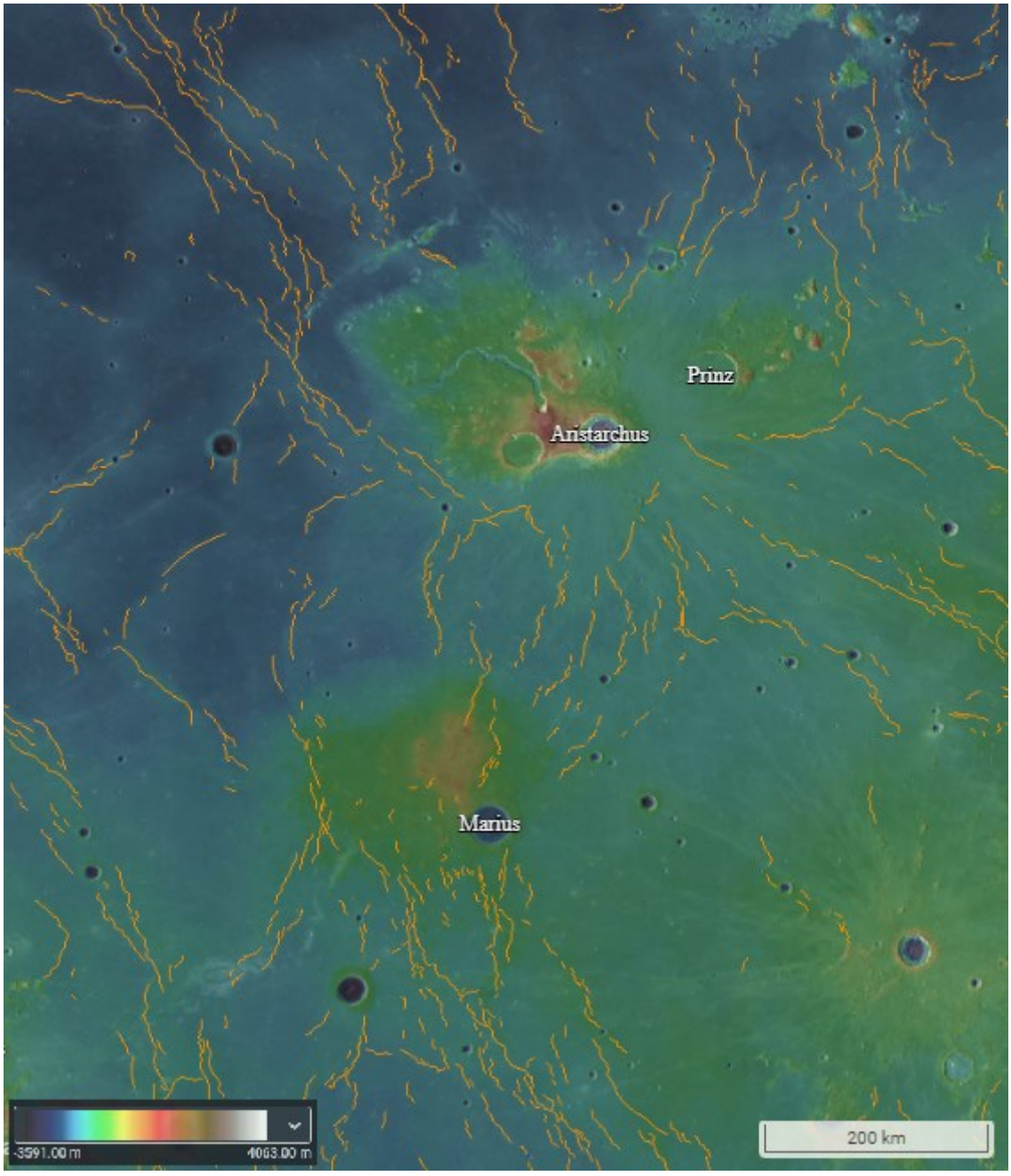

Figure 29. The study area of this work; to the North the Aristarchus Plateau, to the South the Marius Hills complex, in yellow the wrinkle ridges; image taken from quickmap.lroc.asu.edu.

The Marius Hills complex appears as an elongated, elliptical topographic rise, shaped like a shield (**Fig.30**) and it is superposed by 300 small cones, domes, plus numerous sinuous rilles and collapse pits (Spudis et al., 2013). It has an

estimated age between 1.1 Ga and 3.3 Ga, a diameter of 330 kilometres and an average slope of 0.8° (Spudis et al., 2013).

Gravimetry studies (Konopliv et al., 2001) revealed that underneath Marius Hills there should be a big volume of dense subsurface material divided in:

- a northern portion (160-180km in extent).
- a southern portion (100-140 km in extent).

These big gravity anomalies are consistent with the interpretation of Marius as a basaltic shield volcano (Spudis et al., 2013).

The second one (Aristarchus Plateau) has an estimated age of 3.8 Ga, a diameter of 240 kilometres and an average slope of 0.9°. Aristarchus seems to have developed on a structural uplifted highland block and the evidence of massive eruptions are indicated by features like sinuous rilles, among which the most famous example is represented by the 165 km long Vallis Schroteri (Spudis et al., 2013). Spudis et al. (2013) concluded that the Aristarchus-plateau is a proto-volcano which has been arrested during its development.

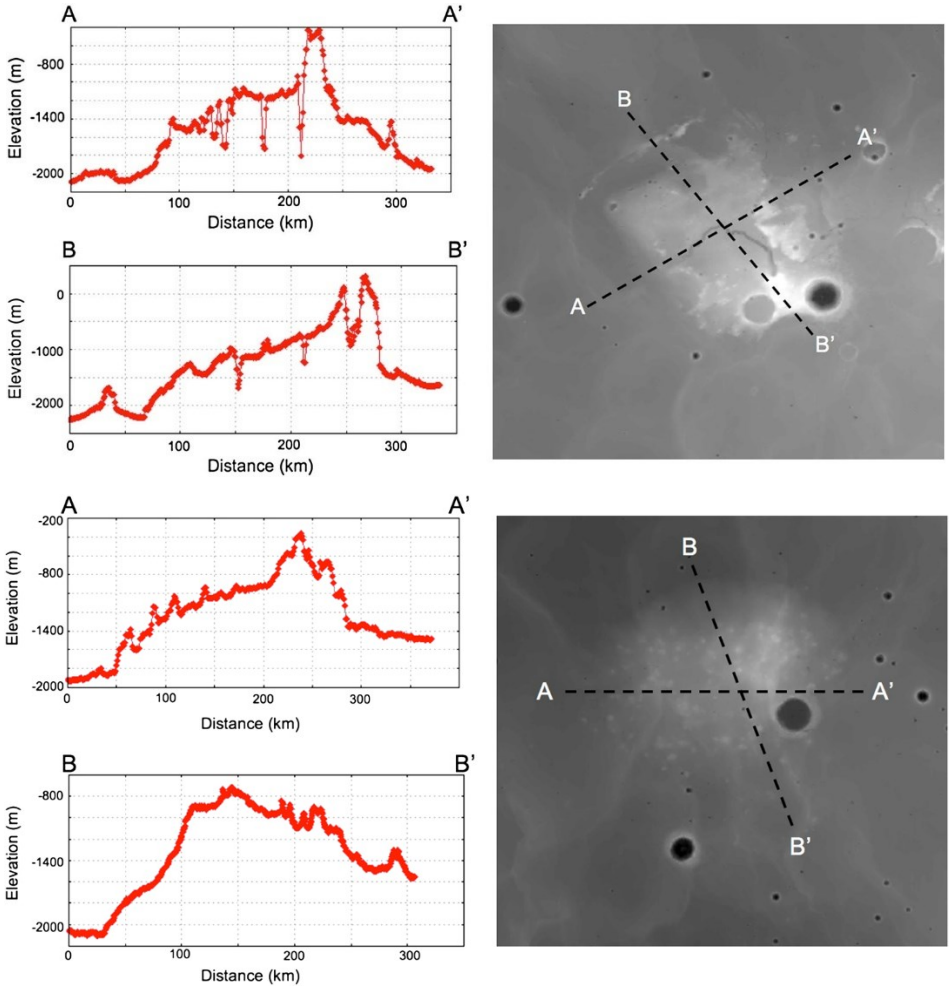

Figure 30. Above image: topographic profiles of the Aristarchus shield; bottom image: topographic profiles of Marius Hills shield. Modified after Spudis et al. (2013).

As **Fig.31** shown Marius Hills is crosscutted by the wrinkle ridges, while this does not happen for the Aristarchus Plateau. The mapping of these structures has been done at global scale (see Fortezzo et al., 2020) or at a very small scale (Lu et al., 2019), but a medium-scale mapping is missing, and this was one of the purposes of this work, along with the calculation of parameters such as the vergence of the wrinkle ridges and the depths of the décollement.

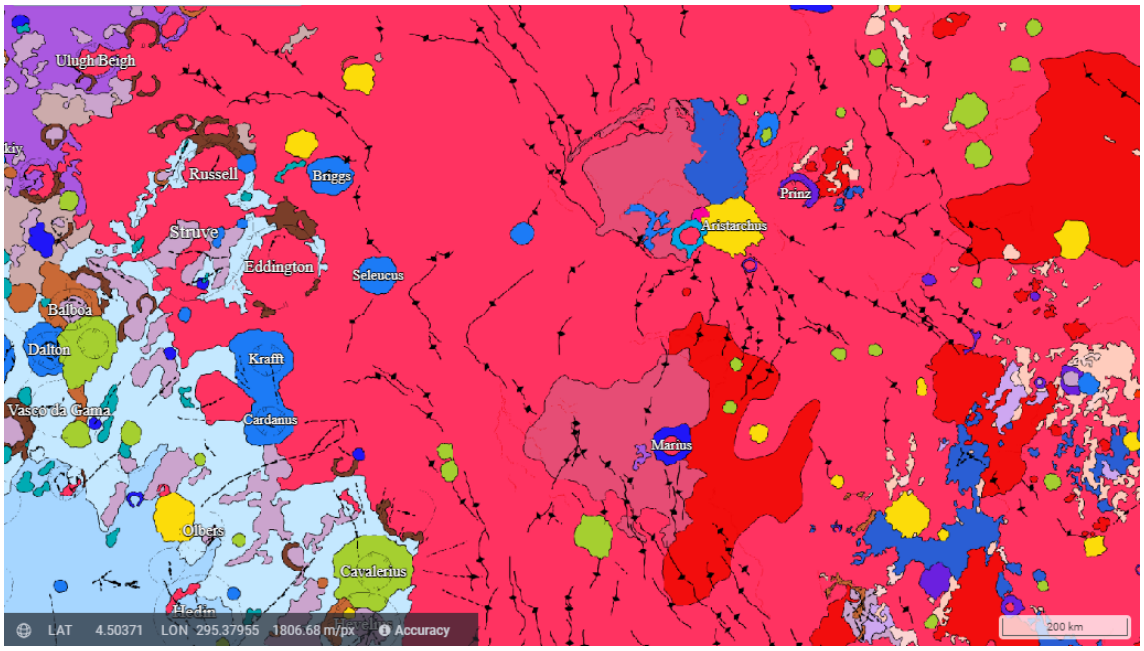

Figure 31. The Unified Geologic map of the Moon with the wrinkle ridges in the region between Marius Hills complex and the Aristarchus Plateau (from Fortezzo et al. (2020).

3. Data

The wrinkles ridges are thrust-fault related landforms with a relief that develops along strike, whereas across strike they show their asymmetry, in fact the forelimb is steeper with respect to the back-limb. Thus, the best product to identify them is a Digital Elevation Model (DEM) (**Fig.32**).

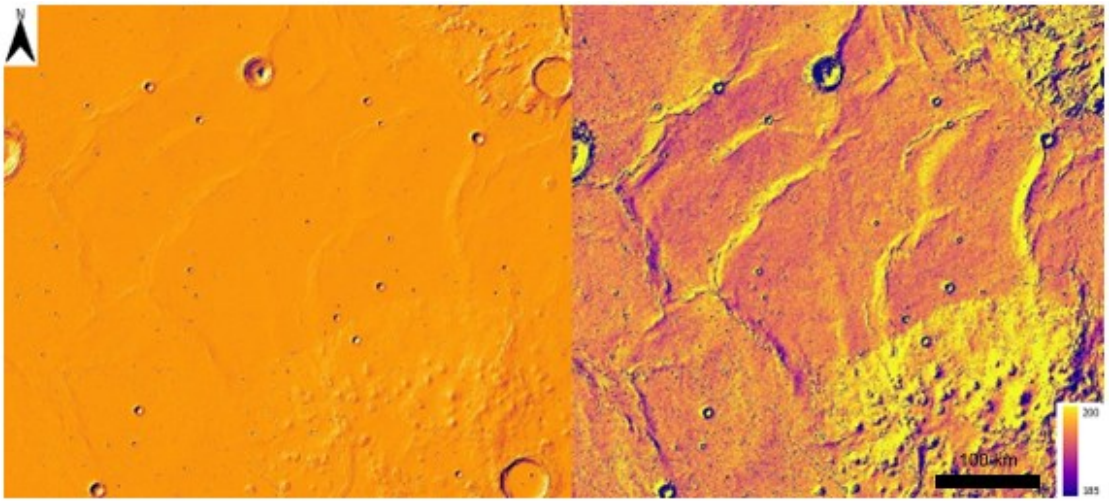

Figure 32. The hill shade derived product derived from the DEM “SLDEM2015”, on the right figure on the bottom right the Marius Hills complex.

For this reason, the following products has been used: the “High-resolution Lunar Topography (SLDEM2015)”. This is a merged product made with the intention of improve the Lunar Orbiter Laser Altimeter (LOLA) coverage by incorporating topographic information from the independently derived and highly complementary Kaguya SELENE Terrain Camera (TC) dataset. SLDEM2015 has a vertical accuracy between 3 and 4 meters and a raster resolution of 236.90 meters (Barker et al., 2016).

LOLA works by propagating a single laser pulse through a Diffractive Optical Element (DOE) that splits it into five beams, which then strike and are backscattered from the lunar surface; for each beam the instrument measures the time of flight, pulse spreading and transmit/return energy (**Fig.33**).

The LOLA, during its activity, has collected over more than 6.5 billion measurements of global surface height with a vertical precision of ~10 cm and an accuracy of ~1m.

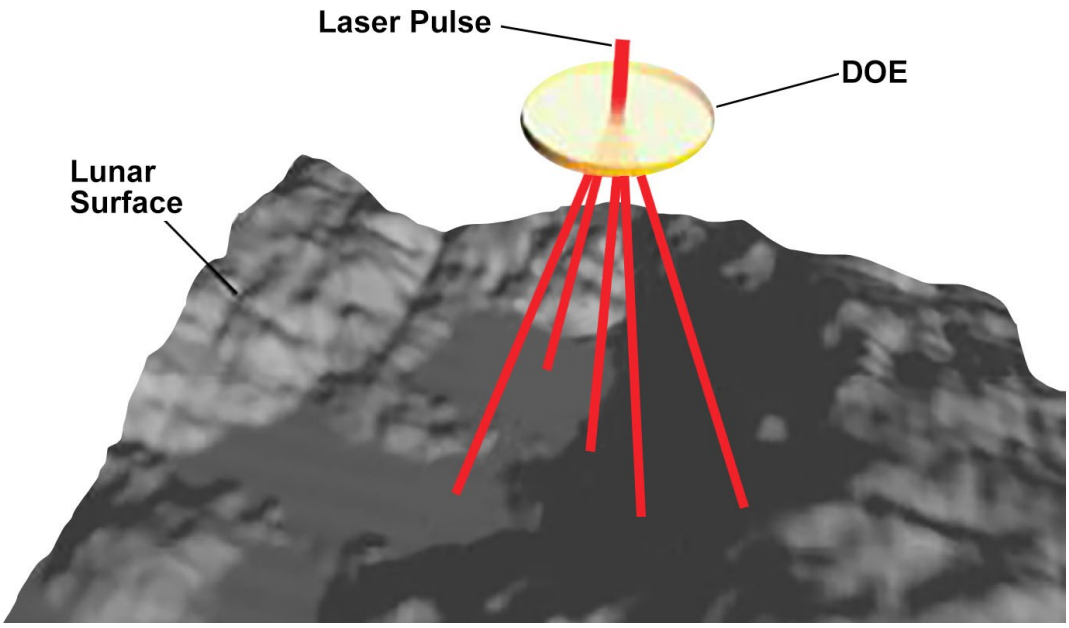

Figure 33. Image showing how LOLA works; taken from https://lunar.gsfc.nasa.gov/lola/.

For more precise analysis KAGUYA (SELENE) TC Derived Data, SLN Terrain Camera Ortho Map Seamless V2.0 (TCORTS) and SLN Terrain Camera DTM Map V2.0 (TCDTMM) have been used.

Kaguya, originally named SELENE (Selenological and Engineering Explorer) is a Japan's mission (operated by JAXA) whose main objective is to create the most detailed topographical model to date. The mission carried two small satellites: Okina and Ouna. Three optical instruments are installed on it: a Terrain Camera (TC), a Multi band Imager (MI) and a Spectral Profiler (SP) (see **Table 1** for instruments specifications).

The Terrain Camera is a push-broom type imager (the image is collected one line at a time, with all the pixels in a line being measured simultaneously) for stereo-pairs observation; TC has two telescopes looking forward and backward to acquire two images of the same location from different angles (stereoscopic view); this allows to obtain Digital Elevation Model (DTM).

	TC	**MI**	**SP**
Spatial Resolution	10m/pixel	VIS: 20 m/pixel, NIR 62m/pixel	562 x 400 m/pixel

FOV (Field of View)	Full mode: 22.4 degrees; Nominal mode: 19.3 degrees; Half mode: 9.65 degrees;	VIS:11 degrees (19.3km); NIR:11.2 degrees (19.6km);	0.23 degrees
Spectroscopic Method	Bandpass filter	Bandpass filter	Diffraction grating
Number of Bands	2(Stereo)	VIS: 5 NIR: 4	296
Band Width	420 nm	10-50 nm	6-8 nm
Wavelength	0.43-0.85 micrometres	VIS: 0.415-0.75-0.9 0.95-1.0 micrometres NIR: 1.0-1.05-1.25-1.55 micrometres	VIS: 0.52-0.96 micrometres NIR1: 0.9-1.7 micrometres NIR2: 1.7-2.6 micrometres

Table 1. Kaguya's instruments specifications; Terrain Camera (TC), Multi band Imager (MI), Spectral Profiler (SP); taken from kaguya.jaxa.jp.

In addition, the Unified Geologic Map of the Moon has been downloaded (1:5M) (Fortezzo et al., 2020) for having a baseline of the current state of lunar geologic knowledge including unit contacts, geologic unit polygons, linear features, and unit and feature nomenclature annotation (**Fig.34**).

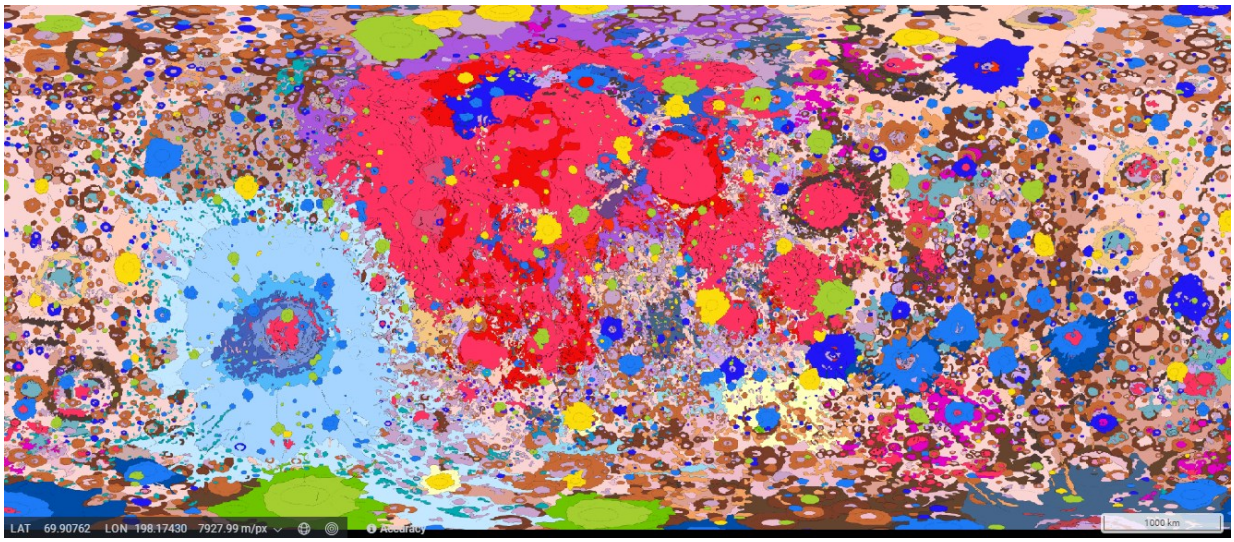

Figure 34. The Unified Geologic Map of the Moon taken from Fortezzo et al. (2020).

4. Methods

To analyse the data, the following software have been used:

- QGIS Desktop 3.28.1
- Minitab
- Microsoft Excel
- MATLAB

The first step was to define a custom Coordinate Reference System (CRS) which is centred on the meridian passing through the centre of Marius Hills and the Aristarchus Plateau (**Fig.35**).

It has been named “Sinusoidal Marius Hills Moon” and it is defined by the following string: **+proj=sinu +lon_0=307 +x_0=0 +y_0=0 +R=1737400 +units=m +no_defs**

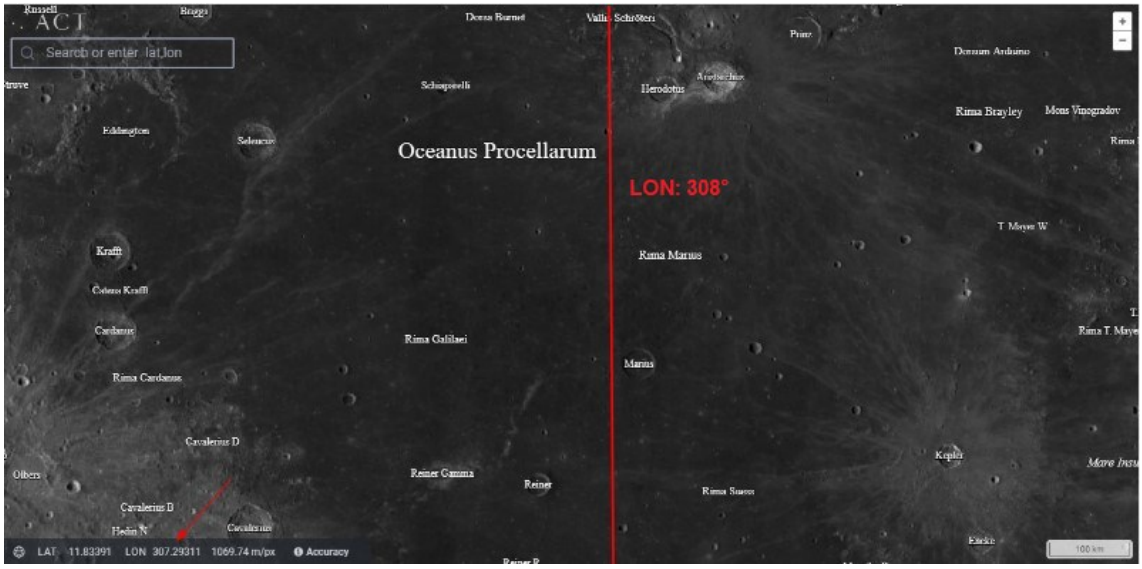

Figure 35. In red the meridian on which is defined the “Sinusoidal Marius Hills Moon” projection.

All the above-mentioned products have been reprojected into this custom-CRS through the QGIS tool “Warp (Reproject)”.

For what concerns the SLDEM2015 and the Unified Geologic Map, these two have been cut thanks to a mask with the dimensions of the area (**bottom left coordinates**: -381410.89,23453.22; **upper right coordinates**: 420025.78,1062027.97) to obtain a more manageable product (**Fig.36**).
On the other hand, the tool “merge raster” has been used to create a raster mosaic starting from the Kaguya tiles and the DEM mentioned above has been used (SLDEM2015) to obtain the hillshade derived product as it has been done for the Kaguya DEM products.

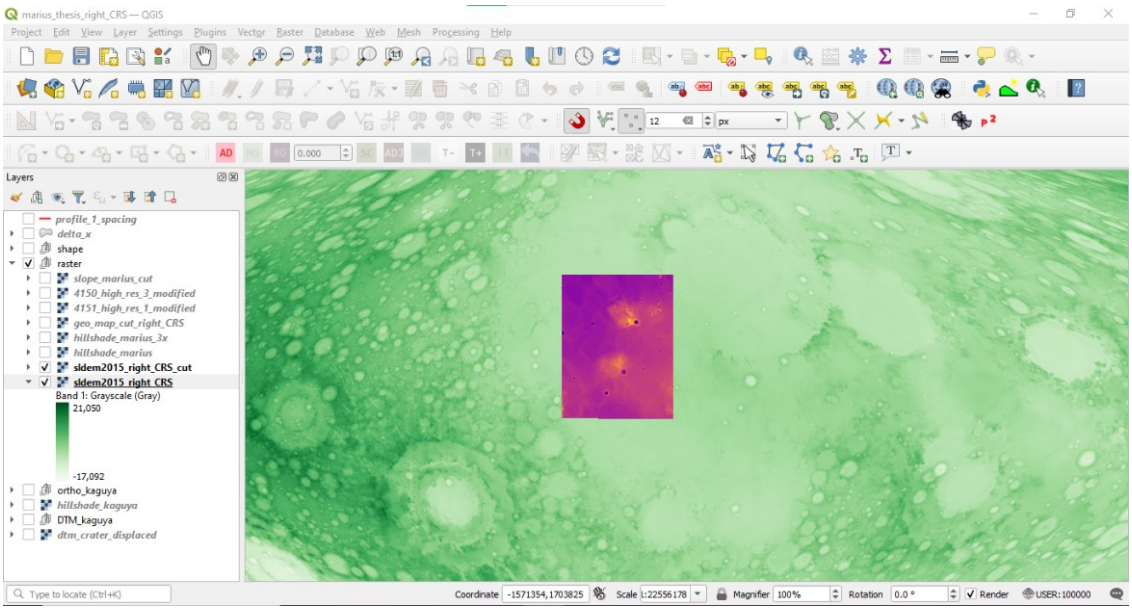

Figure 36. The rectangle is the mask used to cut the geological map and the DEMs.

Regarding the mapping phase, a shapefile with “line-string geometry type” and the “Sinusoidal Marius Hills Moon” CRS has been created.

Then to analyse the geometric properties of the fracture network (i.e., fracture strike, length, and intensity) by using the tool “create grid” (vector creation) a grid with tiles of 100 km * 100 km has been created; for each tile the rose diagram of the ridges has been plotted using the “Line Direction Histogram” plugin and its “tiling” function.

In this framework with “sum length” the length of the ridges in each cell has been summed to calculate the fracture intensity (sum of the length/area of the cell) in the QGIS field calculator.

Since the length of the polylines would serve for further analysis, with another plugin (“Network GT”, a set of tools designed for the geometric and topological analysis of fracture networks.), the length of the ridges was added to the attribute table of the wrinkle ridges shapefile, at a later time these data have been processed using Minitab, a statistical software, and Microsoft Excel to understand their probability distribution and if across the whole dataset it is possible to find families of data described by different distributions of their geometric properties.

The step forward was to investigate the relationship between the maximum displacement and the length of the ridges (D_{max}/L).

While the length of the ridges has been calculated thanks to Network GT, the following relationship has been used to calculate the maximum displacement (D_{max}):

$$D_{max} = \frac{H}{sen\theta}$$

Where **H** is the height and **θ** is the dip of the thrust fault.
H can be measured from the DEM using a plugin (Profile Tool), for this specific purpose the DEM data from Kaguya has been used to minimize the errors.
The measurement procedure of Li et al. (2023) has been applied **(Fig.37**):

1. When it was possible, 10 profiles were drawn perpendicular to the strike of the chosen structure with a distribution as uniform as possible.
2. The relief, defined as the elevation difference between summit and flattened terrain points, was calculated along the ridges and the highest relief was taken.

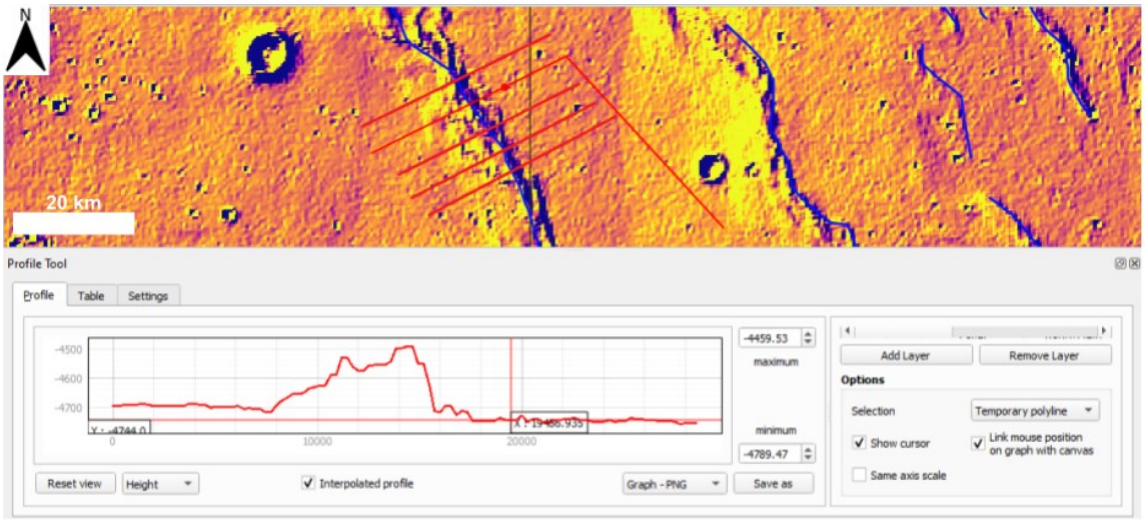

Figure 37. An example of how the procedure of Li et al. (2023) was applied on a wrinkle ridge.

To have several data for a robust statistical analysis some compromises have been accepted. Initially, (i) single ridges (without interaction) and (ii) ridges longer than 10 km have been searched for the mapping, but it wasn't always possible.
In addition, because the most important factor for measuring the D_{max} is the preservation of the ridges (ridges preservation could affect the measurement accuracy), this aspect has been prioritized over the first two (**Fig.38**).

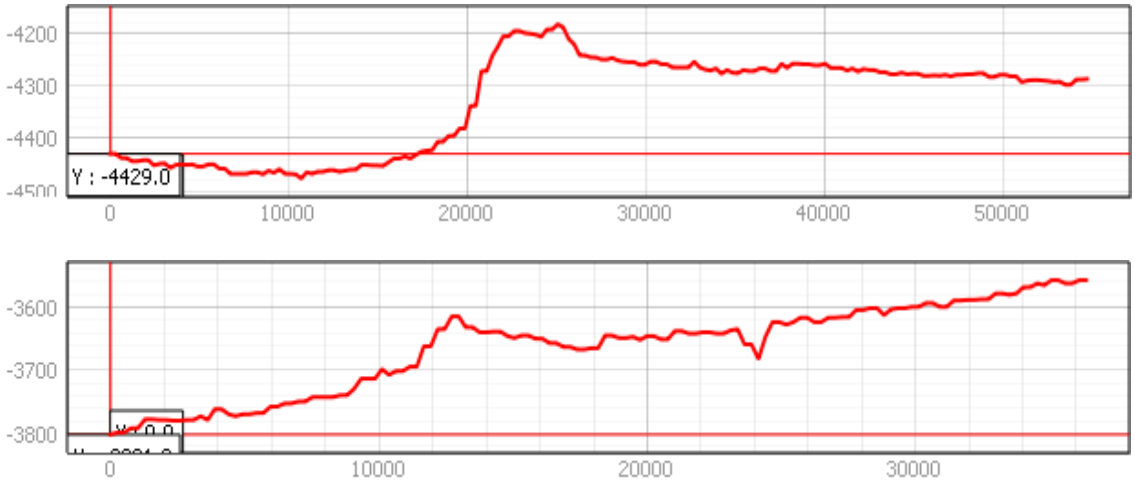

Figure 38. Differences between a well-preserved wrinkle ridge (image above) and another not so well preserved (bottom image)**.**

For better defining the proposed power-law relationship between L and D_{max}, the method developed by Galluzzi et al. (2015) to calculate the true dip of the fault has been used. This method uses displaced crater to calculate the fault geometries and kinematics and is based on the idea that a perfect-initially circular crater if deformed by a fault will have a raised portion and a lowered one, plus, due to the horizontal component of the deformation, the crater will no longer be perfectly circular (**Fig.39**).

Thanks to these two measurable characteristics it is possible to calculate: the slip plunge, displacement, and the true dip of the faults.

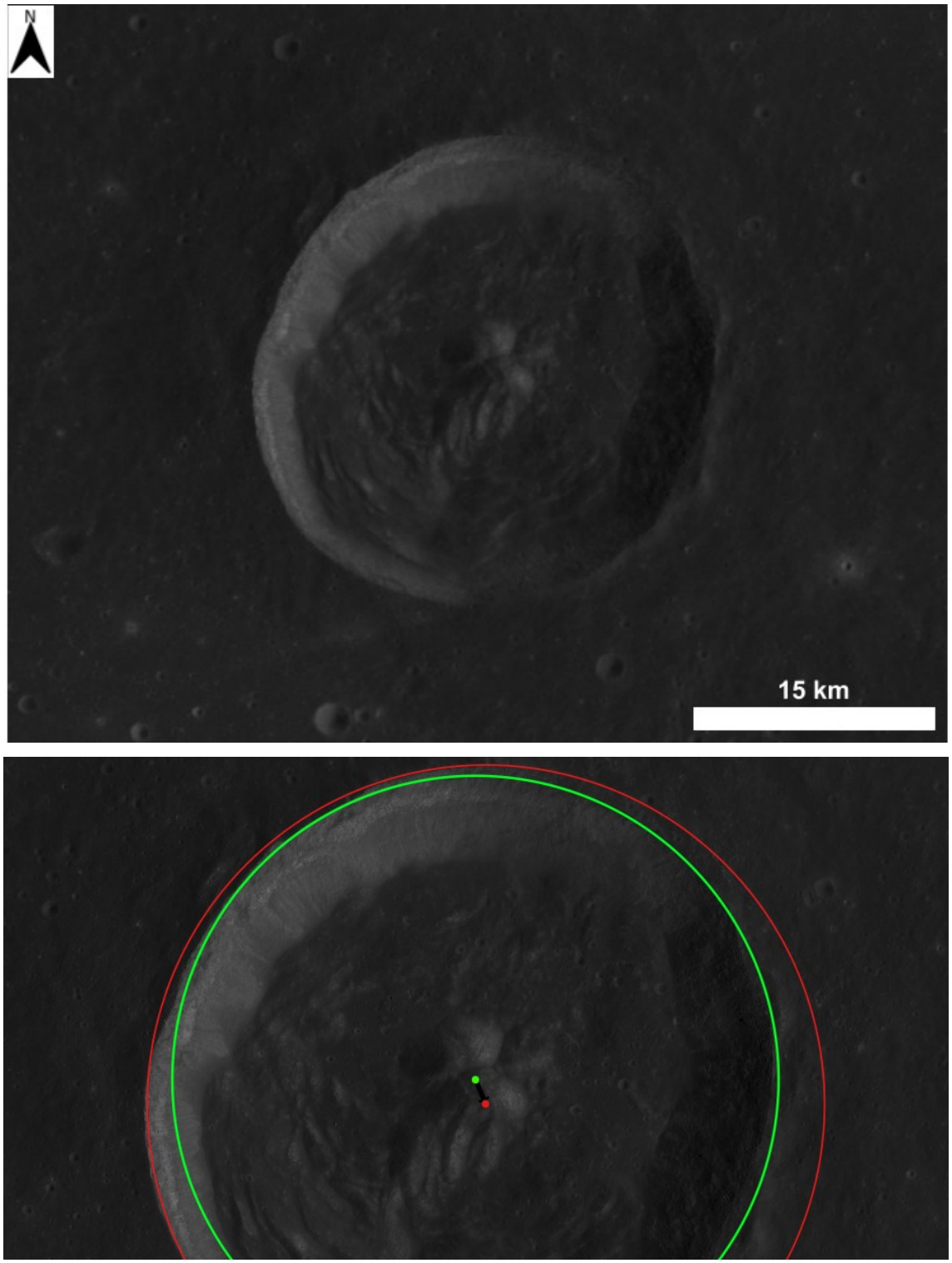

Figure 39. Above image: the displaced crater (coordinates: -59167,210197); bottom image: application of the methology developed by Galluzzi et al. (2014).

Then, the thrusts have been subdivided according by their vergence; the wrinkle ridge morphology is generally characterized by a steeper side (forelimb) which indicates the direction of transport. By using the “profile tool” the steeper side has

been found and the direction of that plane has been calculated by using the plugin QSurf (**Fig.40**).

It has not always been possible to apply this method since sometimes the structure was too degraded to clearly distinguish the forelimb and the back limb.

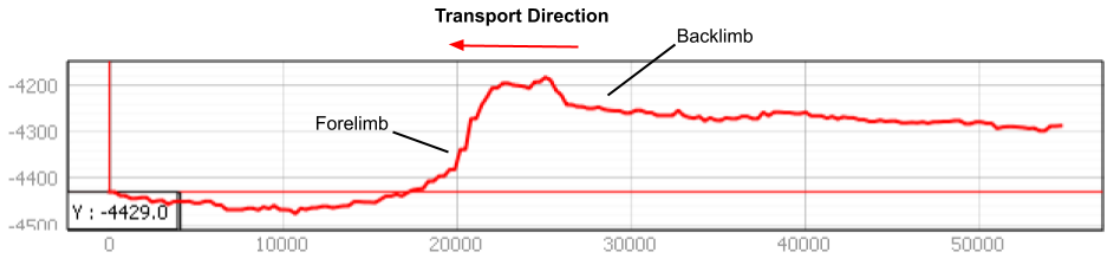

Figure 40. The slope dichotomies between the forelimb and the back limb.

Another important parameter to calculate is the spacing (**Fig.41**), defined as the horizontal distance normal to fault strike between two faults (Schultz et al., 2009).

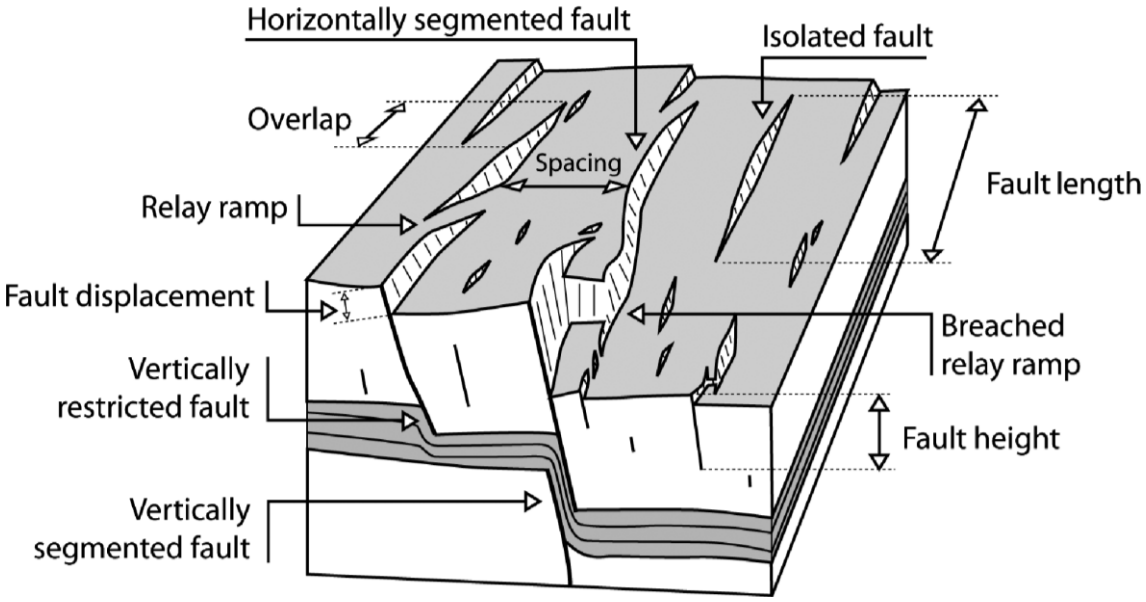

Figure 41. Faults terminology; modified after Schultz et al. (2009).

During this phase is very important to avoid sampling bias, and the following methodology has been adopted:

1. The average strike direction of the family of thrusts in which to derive the spacing has been calculated.

2. Knowing the average strike direction, it has been created a grid of parallel lines with the tool “array of offset parallel lines” with a spacing between the parallel lines of 5 km being the shortest structure of this order of magnitude (**Fig.42**).
3. The right point of intersections has been identified thanks to the tool “line intersections” and with the tool “measure line” the distance between the points of intersection of a structure with the next one has been measured.
4. After collecting all the measures on Microsoft Excel” basic statistical indices, such as the maximum, the minimum, the mean, the median and the standard deviation have been calculated.

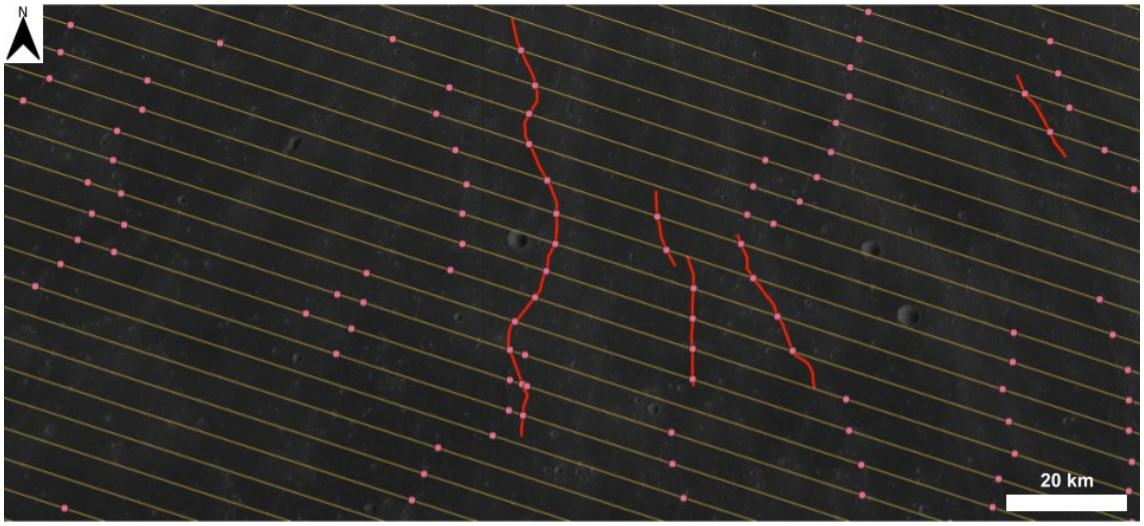

Figure 42. The array of offset parallel lines used to calculate the spacing.

The shortening (S) could be calculated in two different ways.

- It could be calculated with the following equation: $S = h[\frac{1}{\sin\theta} - \frac{1}{\sin(2\gamma-\theta)}]$ where h is the layer thickness, θ is the dip angle of the fault and γ is equal to the back-limb angle γ_i. (**Fig.43**);
- Else, as $S = \cot\theta * H$, where θ is the dip angle of the fault and H is the summit point of the wrinkle ridge.

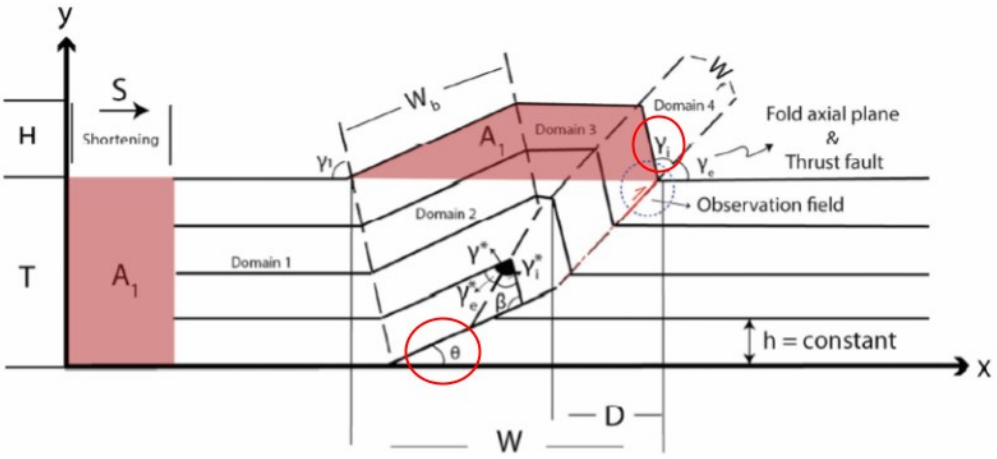

Figure 43. The geometry of a fault-propagation fold; ridge height(H), detachment depth (T), conserved area (A1), dip angle of ramp (θ), horizontal shortening (S), layer thickness (h); the bisecting interlimb angles (γ* = γi* = γe*, if h = constant), the bisecting forelimb angles (γ = γi = γe, if h = constant), back limb dip angle (γ1), forelimb-cut angle (β), and calculated front and back-limb width (Wf & Wb); modified after Karagoz et al. (2022).

The first method is characterized by some limitations, because h (layer thickness) is not known. In the end, the latter method was more reliable because it is based on the height of the structure (the summit point) measured on the DEM and the dip angle of the fault.

After obtaining the spacing and the shortening it has been possible to calculate the original spacing:

$$Original\ Spacing\ (Os) = S_h + S_p$$

Where S_h is the shortening and S_p the mean of the present-day spacing.
The last parameter to calculate was the décollement depth (T), in order to do this the area-conservation principle has been used (**Fig.43**). According to this theory (Epard & Groshong; 1993) T is equal to the uplifted area (A) divided by the shortening (S_h).

$$T = \frac{A}{S_h}$$

Regarding the uplifted area (A), it was calculated with the following methodology derived by Karagoz et al. (2022):

1. A wrinkle ridge characterized by a profile in which the forelimb and the back limb are well-recognizable has been selected;
2. The x-y coordinates of the profile have been exported as a CSV file to Microsoft Excel;
3. The CSV table has been imported in MATLAB and plotted to define a reference level above which the area will be calculated;
4. The cross-sectional area of ridges has been calculated by using a trapezoidal numerical integration (**Figs.44** and **45**).

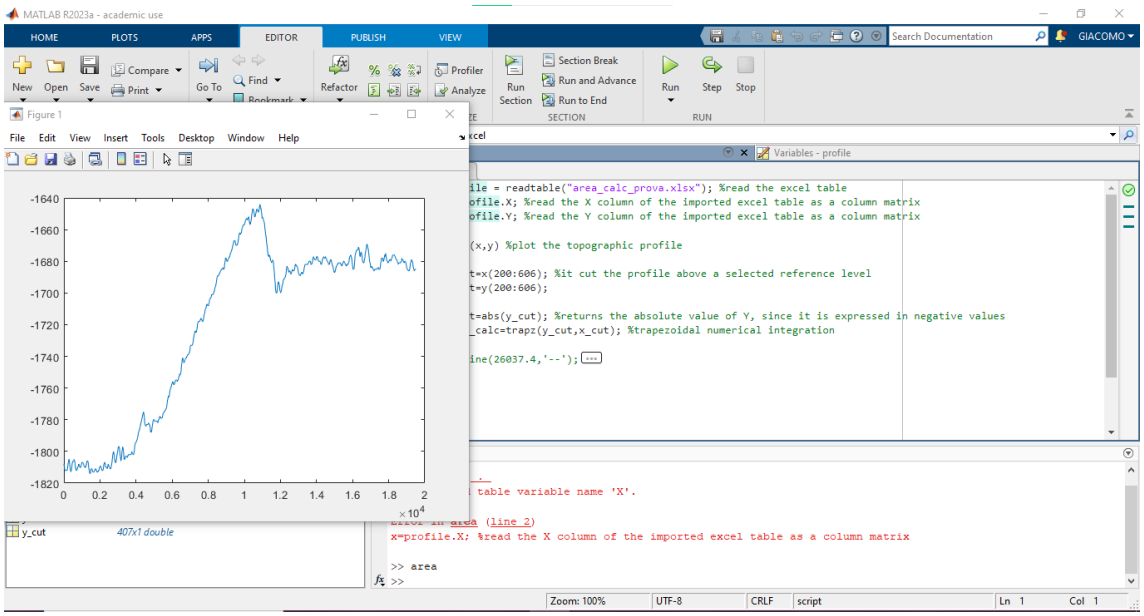

Figure 44. The cross-sectional area of ridges calculated with MATLAB.

```
profile = readtable("area_calc_prova.xlsx"); %read the excel table


x=profile.X; %read the X column of the imported excel table as a
column matrix

y=profile.Y; %read the Y column of the imported excel table as a
column matrix


plot(x,y) %plot the topographic profile

x_cut=x(200:606); %it cut the profile above a selected reference
level

y_cut=y(200:606);


y_cut=abs(y_cut); %returns the absolute value of Y, since it is
expressed in negative values

area_calc=trapz(y_cut,x_cut); %trapezoidal numerical integration
```

Figure 45. The MATLAB code used to calculate the excess area.

5. Results

596 wrinkle ridges have been mapped with length ranging from 1324 meters to 150 km (**Fig.46**).

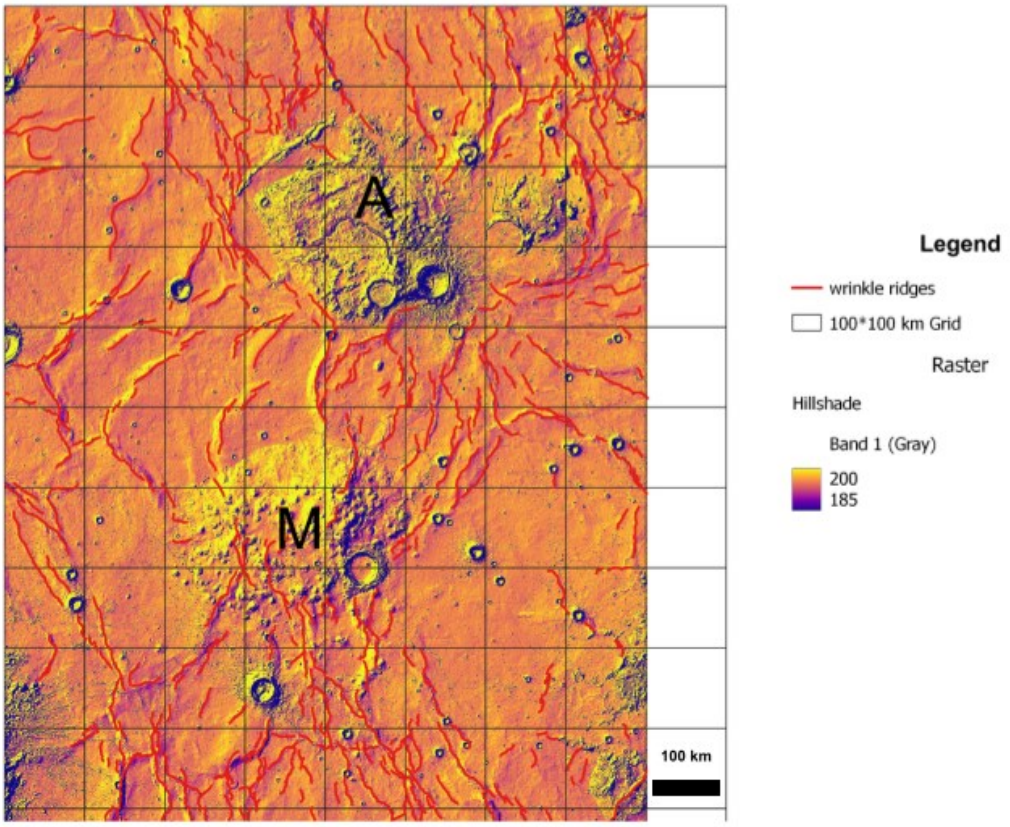

Figure 46. The study area with the mapped wrinkle ridges; the letter A stands for Aristarchus Plateau; the letter M stands for the Marius Hills complex.

For more in-depth analyses, the polylines representing the wrinkle ridges in the structural map have been subdivided into the individual segments that compose them with the tool “Explode”.

As mentioned above the rose diagrams of both the polylines (related to the shapefile ‘wrinkle ridges’) and the single segments of the previous-mentioned polylines have been produced; they are quite similar (**Figs 47** and **48**).

On the other hand, the fracture intensity ranges from 0.000123 to 0.100494 (**Fig.49**).

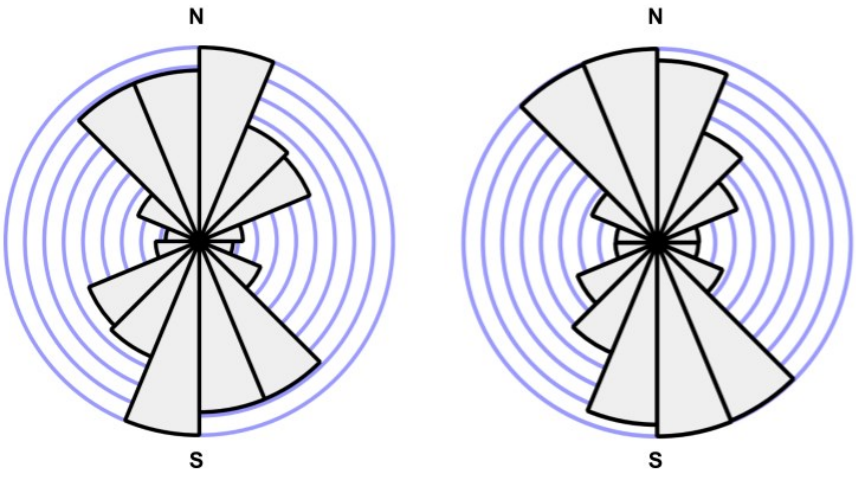

Figure 47. Rose diagrams of the single segments, on the left side the family of wrinkle ridges between 3.5-20 km, on the right side the family between 20-85 km.

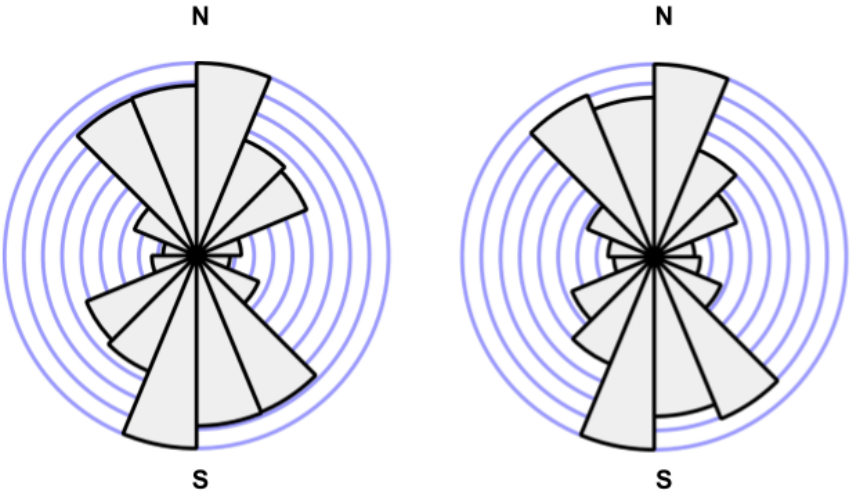

Figure 48. Rose diagrams of the polylines, on the left side the family of wrinkle ridges between 3.5-20 km, on the right side the family between 20-85 km.

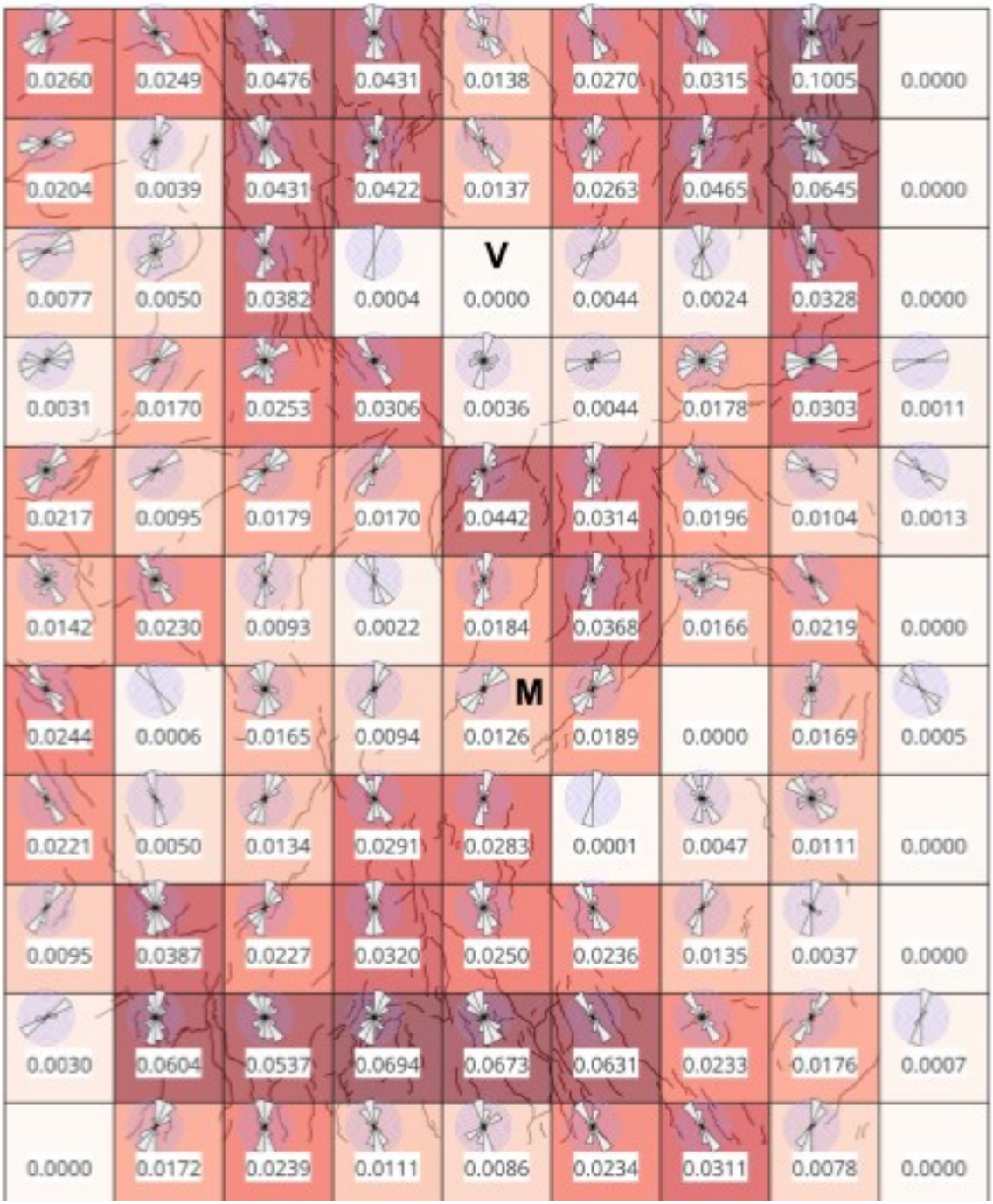

Figure 49. The calculated fracture intensity; the letter V stands for Vallis Schröteri (Aristarchus Plateau), the letter M stands for Marius Crater.

The analysis of length distribution performed with Minitab give as a result a lognormal distribution as can be seen in **figure 50**, thereafter, the length versus the cumulative frequency have been plotted to understand if across the dataset it is possible to find families of data.

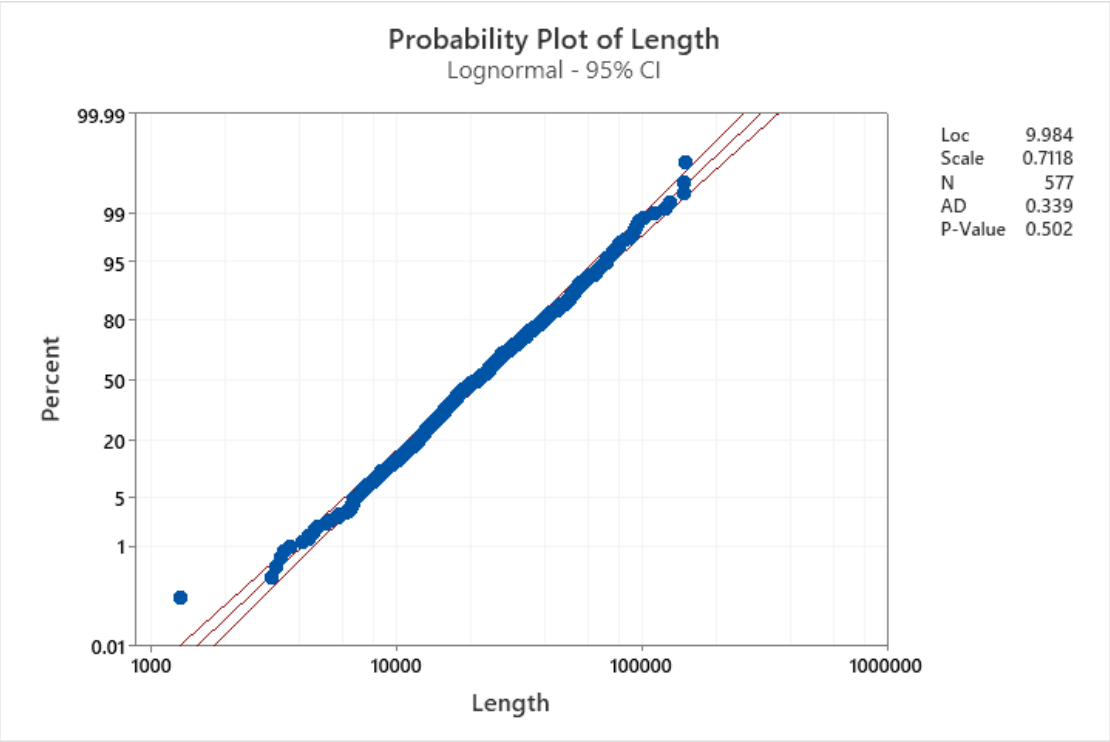

Figure 50. The probability plot of length obtained with Minitab; p-value is the probability of obtaining test results at least as extreme as the result observed, under the assumption that the null hypothesis is correct (in this case there is a high probability to be a log-normal distribution); the Anderson-Darling statistic (AD) measures how well the data follow a particular distribution. For a specified data set and distribution, the better the distribution fits the data, the smaller this statistic will be.

4 families have been identified (**Fig.51**):

1. Below 3.5 kilometres
2. Between 3.5 kilometres and 20 kilometres, defined by the following equation: $y = 1E\text{-}08x^{2.2504}$ - $R^2 = 0.9854$
3. Between 20 kilometres and 84 kilometres, defined by the following equation: $y = 38.02\ln(x) - 325.43$ $R^2 = 0.9709$
4. Above 84 kilometres

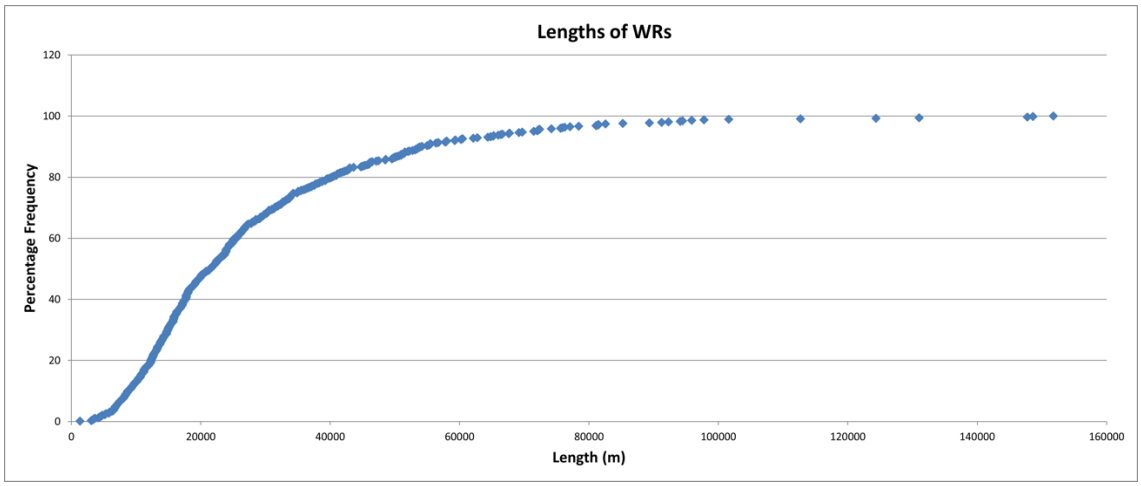

Figure 51. Length versus Cumulative frequency plot.

As mentioned in the **chapter 5** (**Methods)** the methodology developed by Li et al. (2023) has been applied to investigate the relationship between D_{max} and L. If the height (H) can be measured from the Kaguya DEM, conversely the angle (θ) must be assumed. So, the D_{max} has been calculated for 5 different values: 5°, 10°, 20°, 30° and 40°.

The angle which led to more convincing results was θ=20° for three main reasons:

1. Using Finite Element Model, the dip angle of wrinkle ridges on the Moon was estimated to be between 5° and 25° by Byrne et al. (2015).
2. Using the method described by Galluzzi et al. (2015), two displaced craters have been used to infer the true dip angle obtaining as result dips of 14° and 17° (**Table 2**).
3. In addition, plotting the D_{max} calculated with a θ=20° versus the length of the ridges and remembering that the relationship between these two quantities is regulated by γ (scaling factor), a γ=8.3E-3 has been obtained, which is on the same order of magnitude of the value obtained by Li et al (2023) (**Fig.52**).

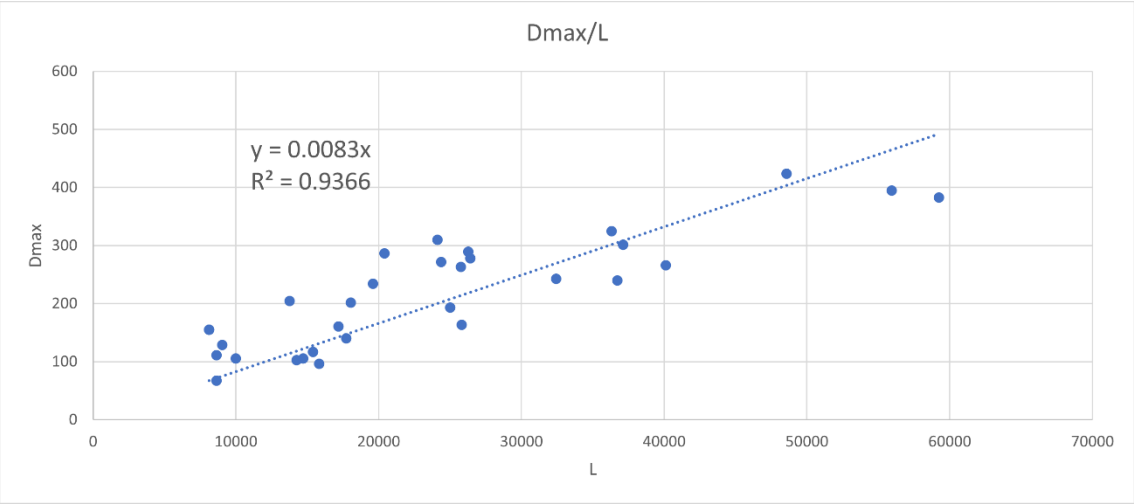

Figure 52. The maximum displacement versus length plot.

Table 2 shows all the values that was possible to calculate for two displaced craters:

Crater (Sinusoidal Marius Hills Moon CRS)	**H_d (m)**	**V_d (m)**	**Slip Plunge (°)**	**Displacement (m)**	**True Dip (°)**	**Strike (N°)**
Crater 1 (156818,451942)	104.311	16	8.72°	105.53	17.05°	48.81°
Crater 2 (-58185,209502)	1238.641	290.6	13.20°	1272.27	14.02°	42.03°

Table 2. Table with all the parameters that it was possible to calculate for the craters as in Galluzzi et al. (2015); H_d is the horizontal component of displacement; V_d the vertical component of displacement.

The next step was to classify the wrinkle ridges by their vergence, unfortunately it was not possible to do this for all the thrusts, but only for 363 out of 596 (**Fig.53**). Then, on QGIS, a different color has been assigned for each different vergence family at 45° intervals (1°-45°; 45°-90°; 90°-135°; 135°-180°; 180°-225°; 225°-270°; 270°-315°; 315°-360°).

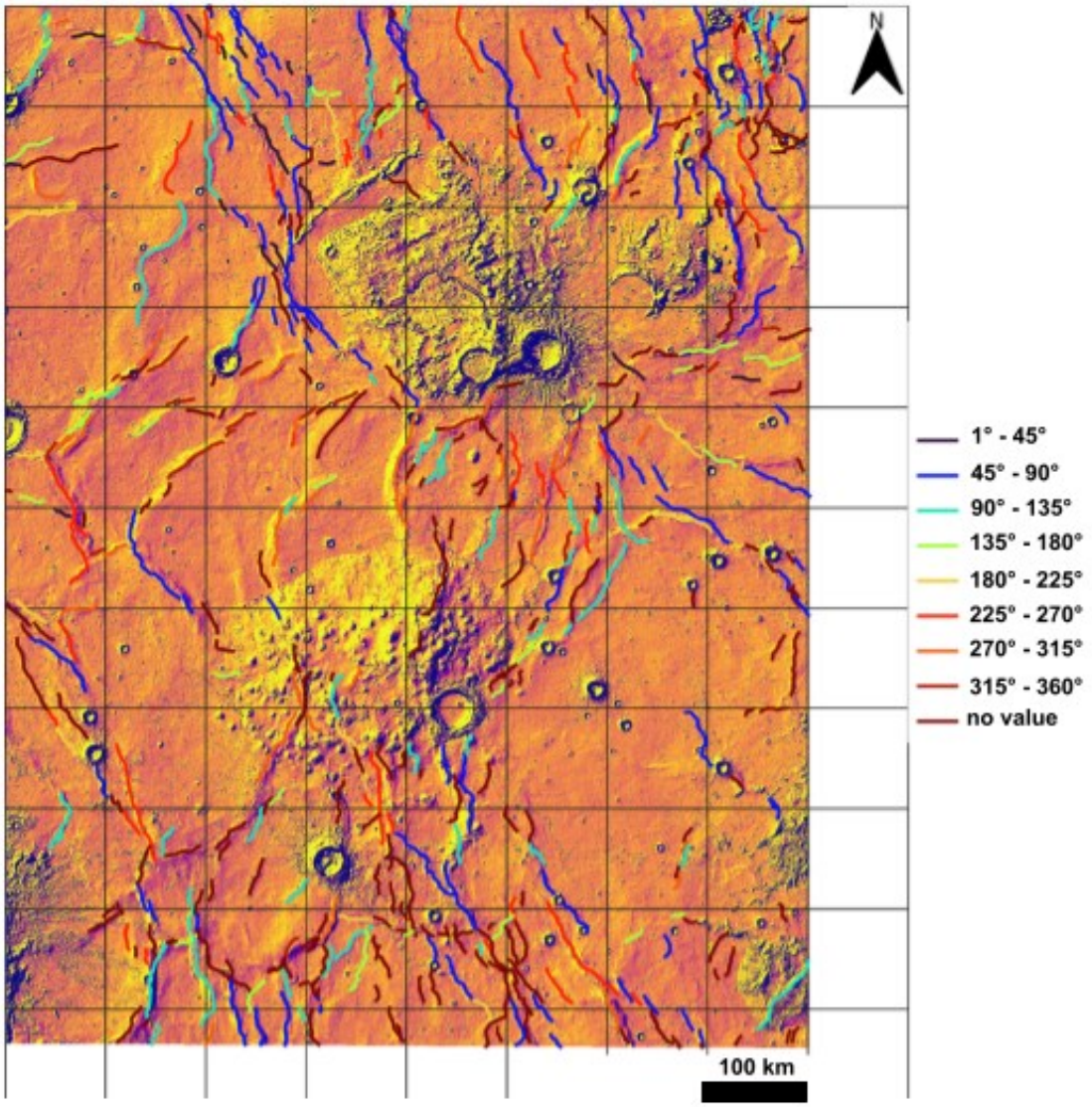

Figure 53. Wrinkle ridges classify by their vergence.

It was also possible to identify systems not only based on their vergence, but also on their spatial distribution, as **figure 54** shown 5 fault systems have been identified:

1. NW fault system (vergence:45°-90°)
2. NW and on the LHS of the Aristarchus Plateau fault system (vergence:45°-90°)
3. SE fault system (vergence:45°-90°)
4. NE fault system (vergence:45°-90°)
5. NE fault system (vergence:225°-270°)

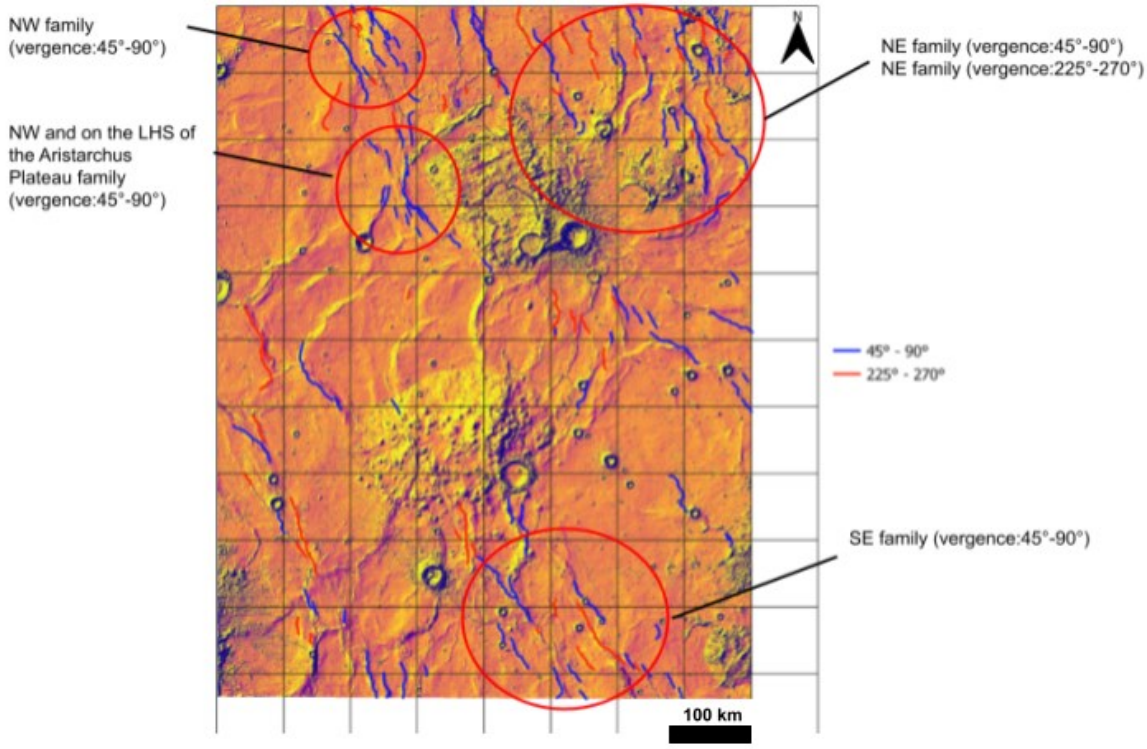

Figure 54. The identified 5 fault systems based on their spatial distribution.

For each fault system seven parameters have been calculated: the maximum, the minimum, the mean, the median, the standard deviation (**Table 3**), the average strike and the original spacing (**Table 4**).

Fault System	Max	Min	Mean	Median	Std. Dev.
NW fault system (vergence:45°- 90°)	64963.9	1780.6	27976.7	27407.3	17625
NW and on the LHS of the Aristarchus Plateau fault system (vergence:45°- 90°)	68006.1	3593.6	22959.4	20001.8	15921.2

SE fault system (vergence:45°- 90°)	131753.5	24548.1	73662.6	57791.8	41628.8
NE fault system (vergence:45°- 90°)	223683.6	10521.6	72563.8	64534.2	53717.8
NE fault system (vergence:225°- 270°)	213267.2	6630.7	89214.7	71843.2	58223.4

Table 3. The maximum, the minimum, the mean, the median and the standard deviation of the spacing (S_p).

Fault System	**Strike(N°)**	**Sp (m)**	**O_s (m)**
NW fault system (vergence:45°- 90°)	135.5	279796.7	28241.4
NW and on the LHS of the Aristarchus Plateau fault system (vergence:45°- 90°)	126	22959.4	23188.5
SE fault system (vergence:45°- 90°)	142.7	73662.6	74014.8
NE fault system (vergence:45°- 90°)	120.5	72563.8	72845
NE fault system (vergence:225°-270°)	127	89214.7	89421.2

Table 4. The average strike, the calculated mean of the spacing (S_p) and the original spacing (O_s).

The calculation of the depths of décollement (T) (inferred by using the methodology in the **Chapter Methods**) showed some limitations since:

- It has been possible to calculate T only for certain wrinkle ridges, which are characterized by the presence of clearly identifiable backlimb and forelimb;
- Structures interpreted during the mapping phase as single segment (due to the raster resolution) are instead composed of several segments. This can be seen from the displacement accumulated by these faults, which is too little compared to their length (according to the linear relationship between D and L).

The final data set consists of 21 solid and checked values that have been extracted and plotted (length versus depth of décollement). These data show a well-defined linear relationship (R^2=0.9491) between T and L (**Fig.55**):

$$y = 0.0597x$$

The derived linear relationship between T and L has been applied for estimating the T values from the respective length (L) for all the 596 wrinkle ridges.

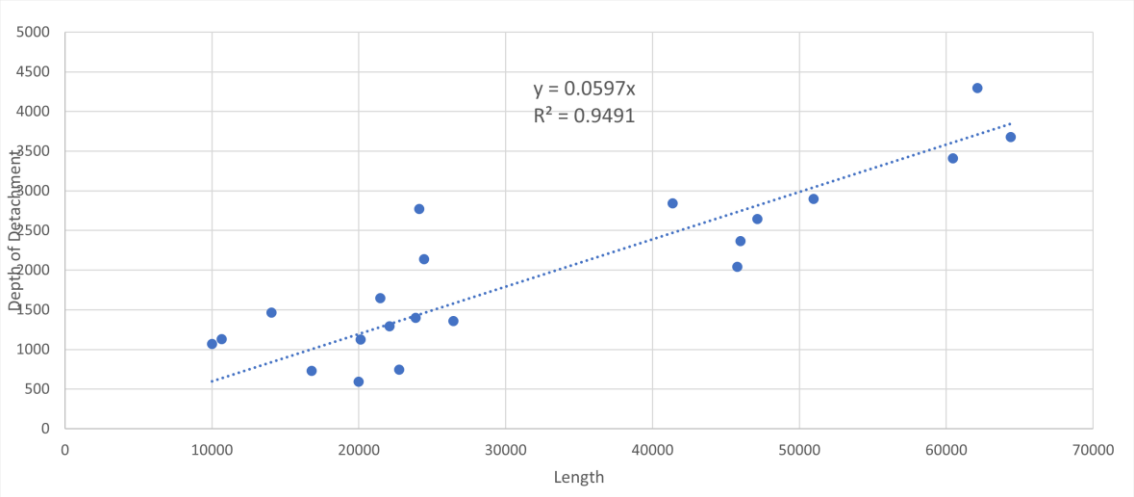

Figure 55. Length versus depth of décollement.

As **figure 56** shown:

- The minimum value is equal to 79 m;
- The 75% of the data is between 797 m and 2029 m;
- The mean is equal to 1634 m.

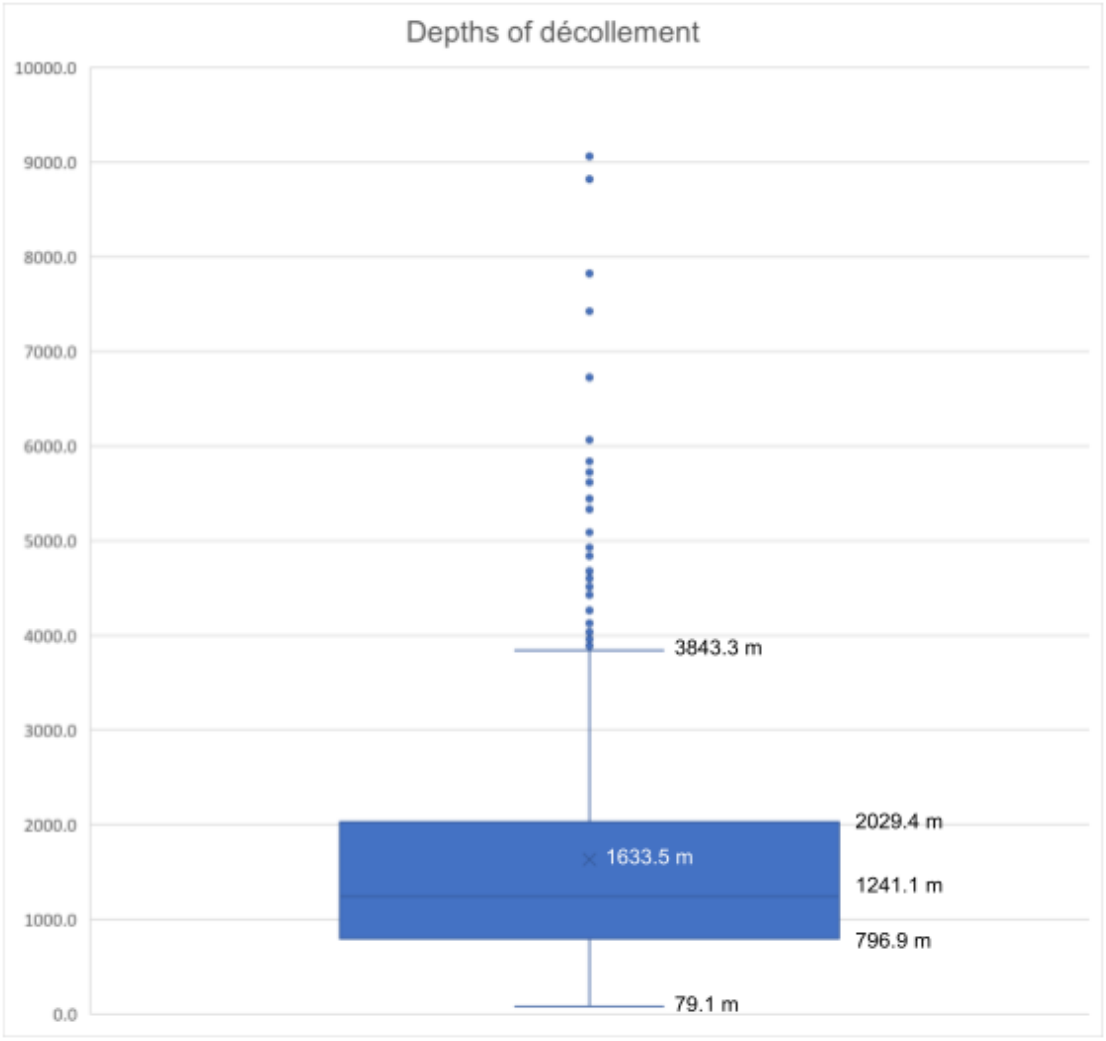

Figure 56. The boxplot showing the range of values of the décollement depth.

The histograms of the depths of décollement by fault system have been created as **figure 57** shown.

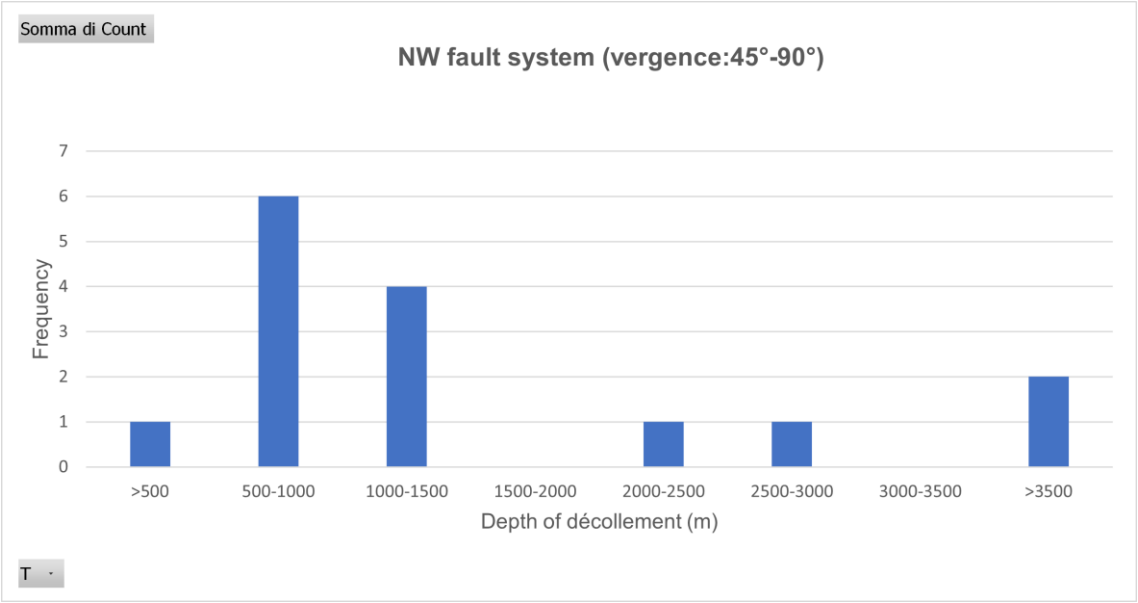
Somma di Count
NW fault system (vergence:45°-90°)
Frequency
0
1
2
3
4
5
6
7
>500
500-1000
1000-1500
1500-2000
2000-2500
2500-3000
3000-3500
>3500
Depth of décollement (m)
T

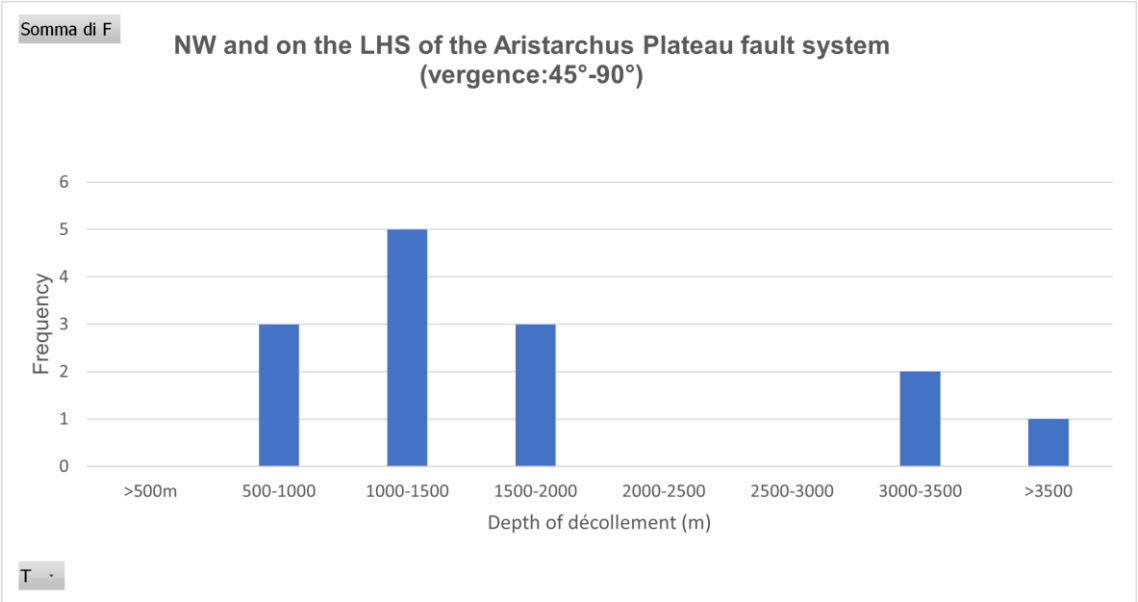
Somma di F
NW and on the LHS of the Aristarchus Plateau fault system (vergence:45°-90°)
Frequency
0
1
2
3
4
5
6
>500m
500-1000
1000-1500
1500-2000
2000-2500
2500-3000
3000-3500
>3500
Depth of décollement (m)
T

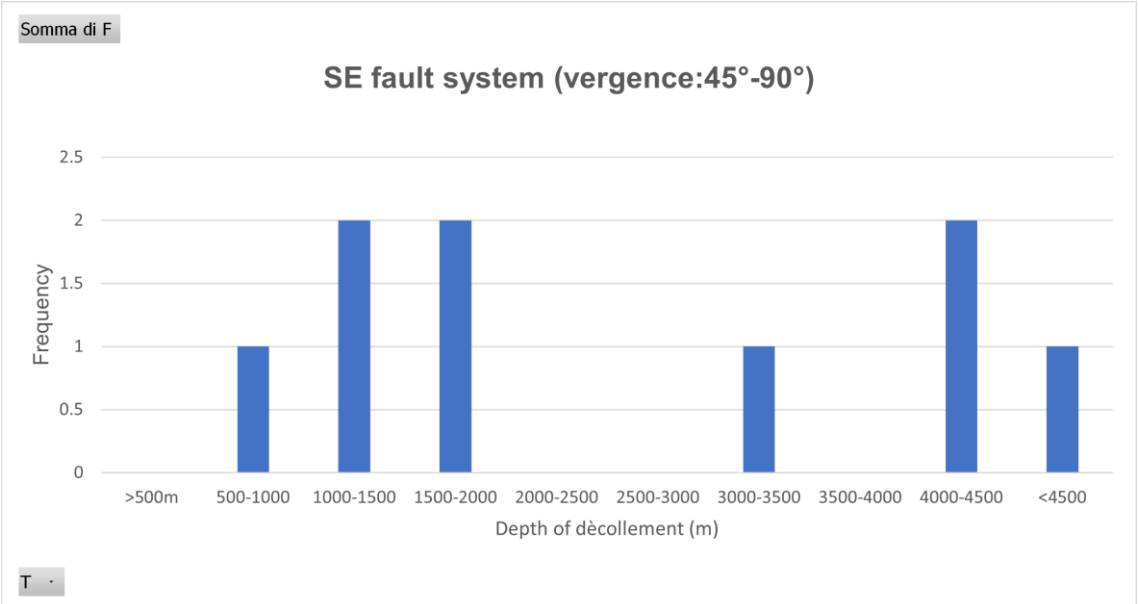
Somma di F
SE fault system (vergence:45°-90°)
Frequency
0
0.5
1
1.5
2
2.5
>500m
500-1000
1000-1500
1500-2000
2000-2500
2500-3000
3000-3500
3500-4000
4000-4500
<4500
Depth of dècollement (m)
T

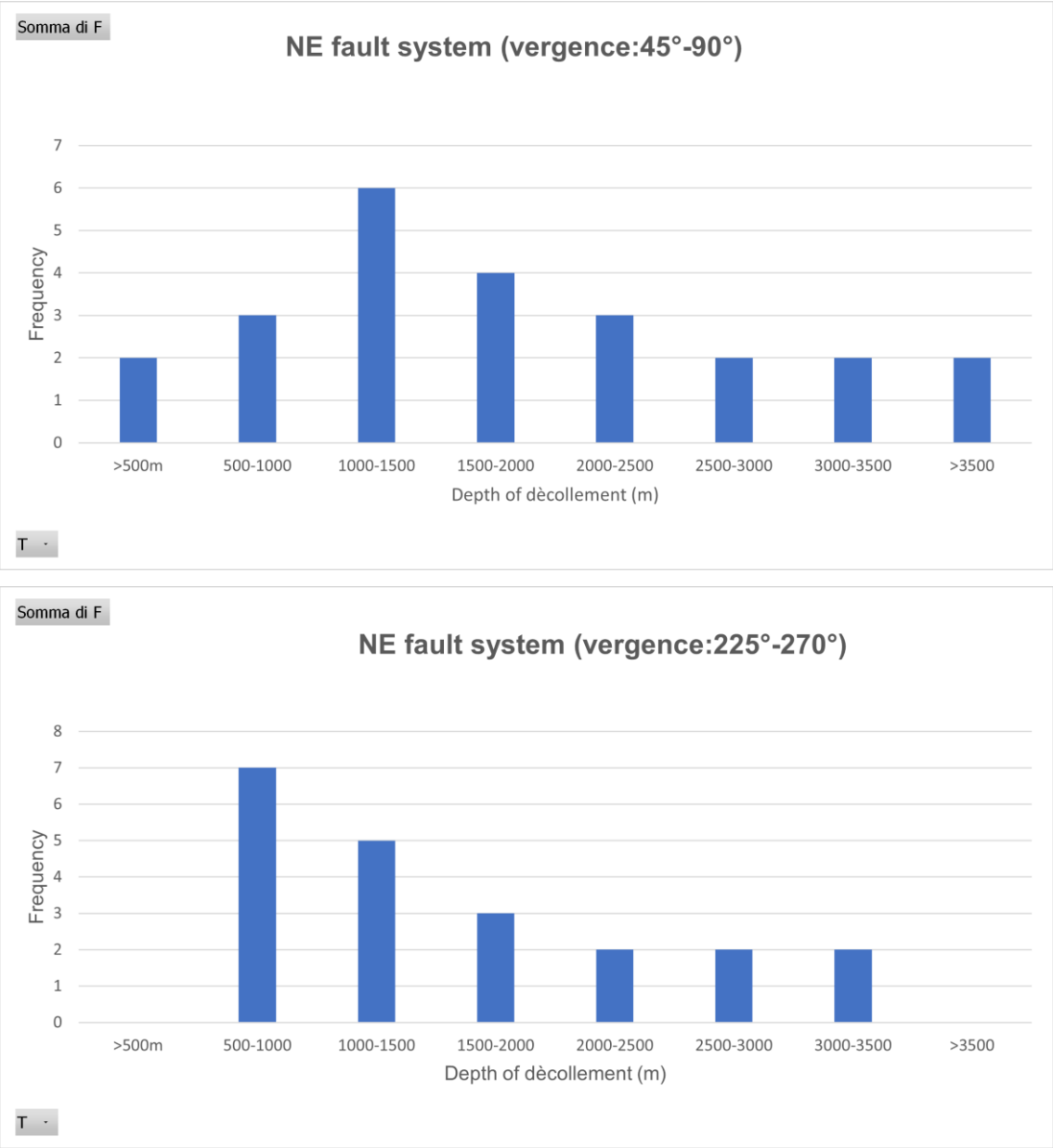

Figure 57. Plot of the depth of décollement based by identified fault system.

6. Discussion

In the previous chapter parameters such as the D_{max}/L relationship, the spacing and the depth of décollement have been calculated and now their geological meaning will be discussed in the framework of the actual geological knowledge of the Moon.

The D_{max}/L values of this work are on the same order of magnitude of those calculated for the whole Oceanus Procellarum. In fact, the scaling factor (γ) estimated in this work is about 8.3E-3, whereas the γ value calculated by Li et al. (2023) was about 10.3E-3.

Furthermore, there is a linear relationship between these D_{max} and L that excludes any lithologic or rheological barrier at depth (Schultz et al., 2010). If there was any vertical restriction the exponent n would change from n=1 to n<1 because the faults would tend to grow laterally while being restricted vertically (Schultz et al., 2010).

The depths of décollement have been inferred thanks to the excess area method. As the boxplot shown in the chapter **Result** (**Fig.56**) the 75% of the result ranges between 796 m and 2090 m (**Fig.58**) which are consistent with those calculated by Lu et al. (2019) in Mare Imbrium, located on the NE border of Oceanus Procellarum, in a relatively small-scale study area (610 m, 800 m, 1100 m, 1320 m, and 2240 m).

These décollement levels indicate the occurrence of horizons of weakness likely related to the presence of paleo-regolith or ejecta layers, formed during hiatus in the volcanic activity of Oceanus Procellarum. Their presence has been confirmed through ground penetrating radar acquisitions, but these surveys reached a depth of the order of a few hundred meters up to a maximum of 1 km (see **Chapter 2.2, Fig.11**) (Bando et al., 2015).

Even if these radar surveys represent a spatial limited datum, it is possible to assume that the mechanical layering due to bodies of lava infillings interleaved by paleo-regolith is present in depth, and it is able to control the development of large-scale wrinkle ridges for two reasons:

1. Depths of décollement greater than 1 km have been calculated in this work using the excess area method;
2. The presence of interruptions in the volcanic activity and the related formation of regolith layers must have also occurred in the past (Zhang et al., 2020).

Fault System	Strike(N°)	Sp (m)	Percentage of T >2 km
NW fault system (vergence:45°- 90°)	135.48	27976.7	26.66%
NW and on the LHS of the Aristarchus Plateau fault system (vergence:45°- 90°)	126.03	22959.4	21.43%
SE fault system (vergence:45°- 90°)	142.68	73662.6	44.44%
NE fault system (vergence:45°-90°)	120.5	72563.8	37.5%
NE fault system (vergence:225°-270°)	126.924	89214.7	28.57%

Table 5. A resume of wrinkle ridges parameters related to each wrinkle ridge systems such as strike, spacing (S_W), strain (ε) and the percentage of décollement (T) deeper than 2 km.

Furthermore, an almost linear relationship exists between the values of depth of décollements and the values of the average spacing across different fault systems. This relationship emerges clearly by comparing the calculated spacing with the percentage of T deeper than 2 km for the different systems (**Table 5**). Therefore, it is possible to conclude that smaller spacing values correspond to shallower décollement levels; conversely higher spacing values correspond to deeper décollement levels (**Fig.57 and Table 5 for details**).

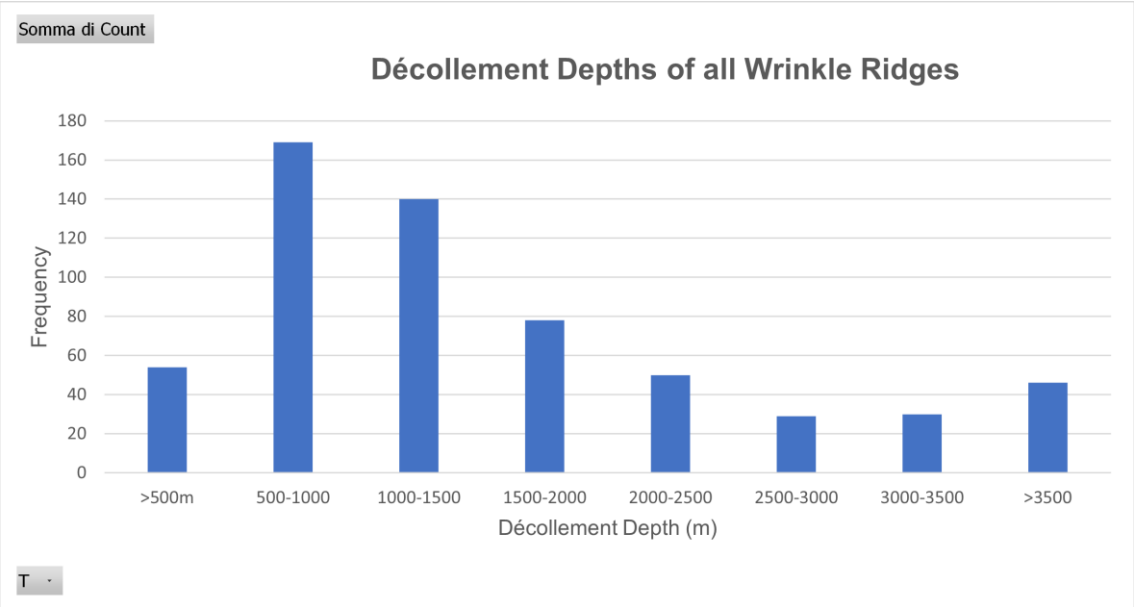

Figure 58. Plot showing that 75% of results are between 500 m and 2000 m.

7. Conclusions

The results of this work can be divided into two macro-categories.

The first concerns the mapping of wrinkle ridges, which has been done at the regional-basin scale; the produced structural map already in itself represents an important outcome since a mapping at this resolution of wrinkle ridges did not exists.

The second one, directly linked to the first one, concerns the application of in-depth structural analyses techniques: the D_{max}/L relationship has been investigated, the spacing and the décollement depths have been calculated. In addition, the latter technique was applied for the first time in Oceanus Procellarum.

Our results are consistent with those reported in the literature being the D_{max}/L values of the same order of magnitude of those calculated by Li et al. (2023) for the whole Oceanus Procellarum, and the décollement depths are on the same order of magnitude of those inferred by Lu et al. (2019) in Mare Imbrium, located on the NE border of Oceanus Procellarum. In addition, we have excluded any subsurface rheological boundary that could affect the growth of the wrinkle ridges, because of the linear relationship between the maximum displacement (D_{max}) and the lengths (L) of these structures.

The most innovative and intriguing aspect of this work is the estimation of the décollement depths, which has never been done in Oceanus Procellarum. The 75% of the result ranges between 796 m and 2090 m (mean:1634 m; median:1241 m; standard deviation:1283) with a linear relationship between the calculated spacing and the depths of detachment. In particular, systems of narrowly spaced wrinkle ridges are characterized by décollement at shallower levels, conversely a family of widely spaced wrinkle ridges are characterized by deeper décollement. These horizons of weakness are likely related to the presence of paleo-regolith or ejecta layers, formed during hiatus in the volcanic activity, which had to be long enough to allow the continuous impact gardening to create a substantial layer of fine regolith.

In the future, it would be interesting to relate, the inferred paleo-regolith layers depths, with the volcanic evolution of Oceanus Procellarum in terms of amount of lava and time of emplacement in function of inferred effusion rate. It would be also of interest to infer how the stress field, responsible of such contractional landforms, evolved through time. This would help us in understanding how the global or regional processes might have driven the deformation of the lunar crust.

References

Andrews-Hanna, J. C., Besserer, J., Head Iii, J. W., Howett, C. J. A., Kiefer, W. S., Lucey, P. J., McGovern, P. J., Melosh, H. J., Neumann, G. A., Phillips, R. J., Schenk, P. M., Smith, D. E., Solomon, S. C., & Zuber, M. T. (2014). Structure and evolution of the lunar Procellarum region as revealed by GRAIL gravity data. Nature, 514(7520), 68–71. https://doi.org/10.1038/nature13697

Bando, Y., Kumamoto, A., & Nakamura, N. (2015). Constraint on subsurface structures beneath Reiner Gamma on the Moon using the Kaguya Lunar Radar Sounder. Icarus, 254, 144–149. https://doi.org/10.1016/j.icarus.2015.03.020

Banks, M. E., Watters, T. R., Robinson, M. S., Tornabene, T. T., Ojha, L., & Williams, N.R. (2012). Morphometric analysis of small-scale lobate scarps on the

Moon using data from the Lunar Reconnaissance Orbiter. JOURNAL OF GEOPHYSICAL RESEARCH, VOL. 117, E00H11, doi:10.1029/2011JE003907.

Barker, M. K., Mazarico, E., Neumann, G. A., Zuber, M. T., Haruyama, J., & Smith, D. E. (2016). A new lunar digital elevation model from the Lunar Orbiter Laser Altimeter and SELENE Terrain Camera. Icarus, 273, 346–355. https://doi.org/10.1016/j.icarus.2015.07.039

Barlow, N. G. (1997). Early Bombardment: Vol. Encyclopedia of Planetary Science. Encyclopedia of Earth Science (Springer, Dordrecht).

Bhutani, R. (2020). Differentiation of the Lunar Interior: Vol. Cudnik, B. (eds) Encyclopedia of Lunar Science. Springer, Cham.

Byrne, P. K., Klimczak, C., McGovern, P. J., Mazarico, E., James, P. B., Neumann, G. A., Zuber, M. T., & Solomon, S. C. (2015). Deep-seated thrust faults bound the Mare Crisium lunar mascon. Earth and Planetary Science Letters, 427, 183–190. https://doi.org/10.1016/j.epsl.2015.06.022

Clark, J. D., Hurtado, J. M., Hiesinger, H., Van Der Bogert, C. H., & Bernhardt, H. (2017). Investigation of newly discovered lobate scarps: Implications for the tectonic and thermal evolution of the Moon. Icarus, 298, 78–88. https://doi.org/10.1016/j.icarus.2017.08.017

Ding, X. Z., & Xu, K. J. (2019, March 18-22). A NEW LUNAR GEOLOGICAL TIME SCALE AND THE GEOLOGICAL EVOLUTION OF THE MOON [Paper presentation]. 50th Lunar and Planetary Science Conference 2019: The Woodlands, Texas, TX, United States.

Epard, J-L., & Groshong, R. H. Jr. (1993). Excess area and depth of detachment. The American Association of Petroleum Geologists Bulletin, V.77, No.8, 1291-1302.

Freed, A.M., Melosh, H.J., Solomon, S.C. (2001). Tectonics of mascon loading: Resolution of the strike-slip faulting paradox. Journal of Geophysical Research, V.106, No.E9, 20603-20620.

Fortezzo, C. M., Spudis, P. D., & Harrel, S. L. (2020, March 16-20). RELEASE OF THE DIGITAL UNIFIED GLOBAL GEOLOGIC MAP OF THE MOON AT 1:5,000,000 [Paper presentation]. 51st Lunar and Planetary Science Conference 2020: The Woodlands, Texas, TX, United States.

Galluzzi, V., Di Achille, G., Ferranti, L., Popa, C., & Palumbo, P. (2015). Faulted craters as indicators for thrust motions on Mercury. Geological Society, London, Special Publications, 401(1), 313–325. https://doi.org/10.1144/SP401.17

Grasemann, B., Exner, U., & Tschegg, C. (2011). Displacement–length scaling of brittle faults in ductile shear. Journal of Structural Geology, 33(11), 1650–1661. https://doi.org/10.1016/j.jsg.2011.08.008

Greenhagen, B. T., Lucey, P. G., Wyatt, M. B., Glotch, T. D., Allen, C. C., Arnold, J. A., Bandfield, J. L., Bowles, N. E., Hanna, K. L. D., Hayne, P. O., Song, E., Thomas, I. R., & Paige, D. A. (2010). Global Silicate Mineralogy of the Moon from the Diviner Lunar Radiometer. Science, 329(5998), 1507–1509. https://doi.org/10.1126/science.1192196

Hauber, E., Mège, D., Platz, T., & Brož, P. (2018). Endogenic Processes. In A. P. Rossi & S. Van Gasselt (Eds.), Planetary Geology (pp. 147–183). Springer International Publishing. https://doi.org/10.1007/978-3-319-65179-8_8

Hiesinger, H. (2003). Ages and stratigraphy of mare basalts in Oceanus Procellarum, Mare Nubium, Mare Cognitum, and Mare Insularum. Journal of Geophysical Research, 108(E7), 5065. https://doi.org/10.1029/2002JE001985

Karagoz, O., Kenkmann, T., & Wulf, G. (2022). Circum-Tharsis wrinkle ridges at Lunae Planum: Morphometry, formation, and crustal implications. Icarus, 374, 114808. https://doi.org/10.1016/j.icarus.2021.114808

Konopliv, A. (2001). Recent Gravity Models as a Result of the Lunar Prospector Mission. Icarus, 150(1), 1–18. https://doi.org/10.1006/icar.2000.6573

Konopliv, A. S., Binder, A. B., Hood, L. L., Kucinskas, A. B., Sjogren, W. L., & Williams, J. G. (1998). Improved Gravity Field of the Moon from Lunar Prospector. Science, 281(5382), 1476–1480. https://doi.org/10.1126/science.281.5382.1476

Lemelin, M., P. G. Lucey, E. Song, & G. J. Taylor (2015), Lunar central peak mineralogy and iron content using the Kaguya Multiband Imager: Reassessment of the compositional structure of the lunar crust, J. Geophys. Res. Planets, 120, 869–887. doi:10.1002/2014JE004778.

Lemelin, M., P. G. Lucey, L.R. Gaddis, T. Hare, and M. Ohtake (2016), Global map products from the Kaguya Multiband Imager at 512 ppd: Minerals, FeO and OMAT, 47th LPSC, abs. #2994.
http://www.hou.usra.edu/meetings/lpsc2016/pdf/2994.pdf

Lemelin, M., P. G. Lucey, K. Miljković, L. R. Gaddis, T. M. Hare, and M. Ohtake (2019), The compositions of the lunar crust and upper mantle: Spectral analysis of the inner rings of lunar impact basins, Planetary and Space Science, 165, 230-243.

Li, C., Li, B., Fu, X., Qiao, L., Ling, Z., Yan, J., Qu, S., & Chen, S. (2023). Analysis of lunar wrinkle ridges regarding the maximum displacement–length scaling relationship and relevant geological factors. Icarus, 391, 115361. https://doi.org/10.1016/j.icarus.2022.115361

Liu, J., & Guo, D. (2018). Lunar Geological Timescale. In B. Cudnik (Ed.), Encyclopedia of Lunar Science (pp. 1–3). Springer International Publishing. https://doi.org/10.1007/978-3-319-05546-6_63-1

Lu, Y., Wu, Y., Michael, G. G., Basilevsky, A. T., & Li, C. (2019). Young wrinkle ridges in Mare Imbrium: Evidence for very recent compressional tectonism. Icarus, 329, 24–33. https://doi.org/10.1016/j.icarus.2019.03.029

Lucey, P. G., Blewett, D. T., & Hawke, B. R. (1998). Mapping the FeO and TiO_2 content of the lunar surface with multispectral imagery. Journal of Geophysical Research: Planets, 103(E2), 3679–3699. https://doi.org/10.1029/97JE03019

McKay, D. S., Heiken, G., Basu, A., Blanford, G., Simon, S., Reedy, R., French, B. M., & Papike, J. (1991). The Lunar Regolith. In G. H. Heiken, D. T. Vaniman & B. M. French (Eds.), Lunar Sourcebook (183-284). Cambridge University Press.

Melosh, H. J. (2011). Planetary Surface Processes (1st ed.). Cambridge University Press. https://doi.org/10.1017/CBO9780511977848

Metzger, P. T., Grundy, W. M., Sykes, M. V., Stern, A., Bell, J. F., Detelich, C. E., Runyon, K., & Summers, M. (2022). Moons are planets: Scientific usefulness versus cultural teleology in the taxonomy of planetary science. Icarus, 374, 114768. https://doi.org/10.1016/j.icarus.2021.114768

Murcray, F. H., Murcray, D. G., & Williams, W. J. (1970). Infrared emissivity of lunar surface features: 1. Balloon-borne observations. Journal of Geophysical Research, 75(14), 2662–2669. https://doi.org/10.1029/JB075i014p02662

Olson, J. E. (2003). Sublinear scaling of fracture aperture versus length: An exception or the rule?: SUBLINEAR SCALING OF FRACTURE APERTURE VERSUS LENGTH. Journal of Geophysical Research: Solid Earth, 108(B9). https://doi.org/10.1029/2001JB000419

Pettit, E., & Nicholson, S. B. (1930). Lunar Temperatures. The Scientific Monthly, 30(6), 558–565. http://www.jstor.org/stable/14730.

Robinson, M. S., Ashley, J. W., Boyd, A. K., Wagner, R. V., Speyerer, E. J., Ray Hawke, B., Hiesinger, H., & Van Der Bogert, C. H. (2012). Confirmation of

sublunarean voids and thin layering in mare deposits. Planetary and Space Science, 69(1), 18–27. https://doi.org/10.1016/j.pss.2012.05.008

Rossi, A. P., Van Gasselt, S., & Hiesinger, H. (2018). The Terrestrial Planets. In A. P. Rossi & S. Van Gasselt (Eds.), Planetary Geology (pp. 249–283). Springer International Publishing. https://doi.org/10.1007/978-3-319-65179-8_11

Schultz, R. A., Soliva, R., Okubo, C. H., & Mège, D. (2009). Fault populations. In T. R. Watters & R. A. Schultz (Eds.), Planetary Tectonics (1st ed., pp. 457–510). Cambridge University Press. https://doi.org/10.1017/CBO9780511691645.011

Shearer, C. K., & Papike, J. J. (1999). Magmatic evolution of the Moon. American Mineralogist, 84(10), 1469–1494. https://doi.org/10.2138/am-1999-1001

Spudis, P. (1993). The Geology of Multi-Ring Impact Basins: The Moon and Other Planets (Cambridge Planetary Science Old). Cambridge: Cambridge University Press. doi:10.1017/CBO9780511564581

Spudis, P. D. (2015). Volcanism on the Moon. In The Encyclopedia of Volcanoes (pp. 689–700). Elsevier. https://doi.org/10.1016/B978-0-12-385938-9.00039-0

Spudis, P. D., McGovern, P. J., & Kiefer, W. S. (2013). Large shield volcanoes on the Moon: LUNAR SHIELD VOLCANOES. Journal of Geophysical Research: Planets, 118(5), 1063–1081. https://doi.org/10.1002/jgre.20059

Stanton-Yonge, A., Cembrano, J., Griffith, W. A., Jensen, E., & Mitchell, T. M. (2020). Self-similar length-displacement scaling achieved by scale-dependent growth processes: Evidence from the Atacama Fault System. Journal of Structural Geology, 133, 103993. https://doi.org/10.1016/j.jsg.2020.103993

Taylor, G.J., Warren, P., Ryder, G., Delano, J., Pieters, C., & Lofgren, G. (1991). Lunar Rocks. In G. H. Heiken, D. T. Vaniman & B. M. French (Eds.), Lunar Sourcebook (183-284). Cambridge University Press.

Watters, T. R. (2022). Lunar Wrinkle Ridges and the Evolution of the Nearside Lithosphere. Journal of Geophysical Research: Planets, 127(3). https://doi.org/10.1029/2021JE007058

Watters, T. R., & Robinson, M. S. (1997). Radar and photoclinometric studies of wrinkle ridges on Mars. Journal of Geophysical Research: Planets, 102(E5), 10889–10903. https://doi.org/10.1029/97JE00411

Watters, T. R., Robinson, M. S., Beyer, R. A., Banks, M. E., Bell, J. F., Pritchard, M. E., Hiesinger, H., Van Der Bogert, C. H., Thomas, P. C., Turtle, E. P., & Williams, N. R. (2010). Evidence of Recent Thrust Faulting on the Moon Revealed by the Lunar Reconnaissance Orbiter Camera. Science, 329(5994), 936–940. https://doi.org/10.1126/science.1189590

Watters, T. R., Robinson, M. S., Collins, G. C., Banks, M. E., Daud, K., Williams, N. R., & Selvans, M. M. (2015). Global thrust faulting on the Moon and the influence of tidal stresses. Geology, 43(10), 851–854. https://doi.org/10.1130/G37120.1

Wei, Z., He, H., Sun, W., Zhuang, Q., & Liang, Z. (2020). Investigating thrust-fault growth and segment linkage using displacement distribution analysis in the active Duzhanzi thrust fault zone, Northern Tian Shan of China. Journal of Structural Geology, 133, 103990. https://doi.org/10.1016/j.jsg.2020.103990

Weider, S. Z., Crawford, I. A., & Joy, K. H. (2010). Individual lava flow thicknesses in Oceanus Procellarum and Mare Serenitatis determined from Clementine multispectral data. Icarus, 209(2), 323–336. https://doi.org/10.1016/j.icarus.2010.05.010

McKay, D. S., Heiken, G., Basu, A., Blanford, G., Simon, S., Reedy, R., French, B. M., & Papike, J. (1991). The Lunar Regolith. In G. H. Heiken, D. T. Vaniman & B. M. French (Eds.), Lunar Sourcebook (183-284). Cambridge University Press.

Whitaker, E. A. (1981), The lunar Procellarum basin. In P. H. Schultz & R. B. Merrill (Eds.), Multi-ring Basins, Proc. Lunar Planet. Sci. (105-111). Printed in U.S.A.

Wieczorek, M. A., & Phillips, R. J. (2000). The “Procellarum KREEP Terrane”: Implications for mare volcanism and lunar evolution. Journal of Geophysical Research: Planets, 105(E8), 20417–20430. https://doi.org/10.1029/1999JE001092

Wilhelms, D. E., & McCauley, J. F. (1971). GEOLOGIC MAP OF THE NEAR SIDE OF THE MOON. Prepared for the National Aeronautics and Space Administration by U.S. Department of the Interior, U.S. Geological Survey.

Wilhelms, D. E., McCauley, J. F., & Newell, J. T. (1987). The geologic history of the Moon. Professional Paper 1348. https://doi.org/10.3133/pp1348

Yue, Z., Michael, G. G., Di, K., & Liu, J. (2017). Global survey of lunar wrinkle ridge formation times. Earth and Planetary Science Letters, 477, 14–20. https://doi.org/10.1016/j.epsl.2017.07.048

Zhang, L., Li, J., Zeng, Z., Xu, Y., Liu, C., & Chen, S. (2020). Stratigraphy of the Von Kármán Crater Based on Chang'E-4 Lunar Penetrating Radar Data. Geophysical Research Letters, 47, https://doi.org/ 10.1029/2020GL088680